

1
2
3
4
5
6
7
8
9
10
11
12
13
14
15
16
17
18

Non-Gaussian statistics in global atmospheric dynamics: a study with a 10240-member ensemble Kalman filter using an intermediate AGCM

Keiichi KONDO^{1, 2} and Takemasa MIYOSHI^{1, 3, 4, 5, 6}

¹RIKEN Center for Computational Science, Kobe, Japan

²Meteorological Research Institute, Japan Meteorological Agency, Tsukuba, Japan

³RIKEN Cluster for Pioneering Research, Kobe, Japan

⁴RIKEN interdisciplinary Theoretical and Mathematical Sciences Program, Kobe, Japan

⁵Department of Atmospheric and Oceanic Science, University of Maryland, College Park,
Maryland, USA

⁶Japan Agency for Marine-Earth Science and Technology, Yokohama, Japan

Correspondence to: Keiichi Kondo (Email: keiichi.kondo@riken.jp)

19 **Abstract.**

20 We previously performed local ensemble transform Kalman filter (LETKF) experiments with up to
21 10240 ensemble members using an intermediate atmospheric general circulation model (AGCM).
22 While the previous study focused on the impact of localization on the analysis accuracy, the present
23 study focuses on the probability density functions (PDFs) represented by the 10240-member
24 ensemble. The 10240-member ensemble can resolve the detailed structures of the PDFs and indicates
25 that non-Gaussianity is caused in those PDFs by multimodality and outliers. The results show that the
26 spatial patterns of the analysis errors are similar to those of non-Gaussianity. While the outliers appear
27 randomly, large multimodality corresponds well with large analysis error, mainly in the tropical
28 regions and storm track regions where highly nonlinear processes appear frequently. Therefore, we
29 further investigate the lifecycle of multimodal PDFs, and show that the multimodal PDFs are mainly
30 generated by the on-off switch of convective parameterization in the tropical regions and by the
31 instability associated with advection in the storm track regions. Sensitivity to the ensemble size
32 suggests that approximately 1000 ensemble members be necessary in the intermediate AGCM-
33 LETKF system to represent the detailed structures of the non-Gaussian PDF such as skewness and
34 kurtosis; the higher-order non-Gaussian statistics are more vulnerable to the sampling errors due to a
35 smaller ensemble size.

36 **1 Introduction**

37 Data assimilation is a statistical approach to estimate a posterior probability density function (PDF) using
38 information of a prior PDF and observations. Based on the posterior PDF estimate, the optimal initial state is
39 given for numerical weather prediction (NWP). The ensemble Kalman filter (EnKF; Evensen 1994)
40 is an ensemble data assimilation method based on the Kalman filter (Kalman 1960) and approximates
41 the background error covariance matrix by an ensemble of forecasts. The EnKF can explicitly
42 represent the PDF of the model state, where the ensemble size is essential because the sampling error
43 contaminates the PDF represented by the ensemble. Although the sampling error is reduced by
44 increasing the ensemble size, the EnKF is usually performed with a limited ensemble size up to
45 $O(100)$ due to the high computational cost of ensemble model runs. Recently, EnKF experiments with
46 a large ensemble have been performed using powerful supercomputers. Miyoshi et al. (2014; hereafter
47 MKI14) implemented a 10240-member EnKF with an intermediate atmospheric general circulation
48 model (AGCM) known as the Simplified Parameterizations, Primitive Equation Dynamics model
49 (SPEEDY; Molteni 2003), and found meaningful long-range error correlations. In addition, they
50 reported that sampling errors in the error correlation were reduced by increasing the ensemble size.
51 Further, Miyoshi et al. (2015) assimilated real atmospheric observations with a realistic model known
52 as the Nonhydrostatic Icosahedral Atmospheric Model (NICAM; Tomita and Satoh 2004; Satoh et al.
53 2008; 2014) using an EnKF with 10240 members. Kondo and Miyoshi (2016; hereafter KM16)
54 investigated the impact of covariance localization on the accuracy of analysis using a modified
55 version of the MKI14 system.

56 MKI14 also focused on the PDF and reported strong non-Gaussianity, such as a bimodal PDF.
57 Previous studies investigated the impact of non-Gaussianity on the EnKF. Anderson (2010) reported
58 that an N -member ensemble could contain an outlier and a cluster of $N-1$ ensemble members under
59 nonlinear scenarios using the ensemble adjustment Kalman filter (EAKF; Anderson 2001). Anderson
60 (2010) called this phenomenon ensemble clustering (EC), which leads to degradation of analysis
61 accuracy. Amezcua et al. (2012) investigated EC with the ensemble transform Kalman filter (ETKF;
62 Bishop et al. 2001) and local ensemble transform Kalman filter (LETKF; Hunt et al. 2007), and found
63 that random rotations of the ensemble perturbations could avoid EC. Posselt and Bishop (2012)
64 explored the non-Gaussian PDF of microphysical parameters using an idealized one-dimensional
65 (1D) model of deep convection and showed that the non-Gaussianity of the parameter was generated
66 by nonlinearity between the parameters and model output.

67 Using the precious dataset of KM16 with 10240 ensemble members, we can make various
68 investigations such as non-Gaussian statistics and sampling errors in the background error covariance.
69 Here we focus on the non-Gaussian statistics in this study. Since the Gaussian assumption makes the
70 minimum variance estimator of the EnKF coincide with the maximum likelihood estimator, the non-
71 Gaussian PDF may bring some negative impacts on the LETKF analysis. KM16 showed that the
72 improvement in the tropics was relatively small by increasing the ensemble size up to 10240, and
73 suggested that the small improvement be related to the convectively dominated tropical dynamics.
74 This study aims to investigate the non-Gaussian statistics of the atmospheric dynamics in more detail
75 to investigate the relationship between the analysis error and the non-Gaussian PDF, as well as the

behavior and lifecycle of the non-Gaussian PDF. To the best of the authors' knowledge, this is the first study investigating the non-Gaussian PDF using a 10240-member ensemble of an intermediate AGCM. This study also discusses how many ensemble members are necessary to represent non-Gaussian PDF without contamination by the sampling error, since in general higher-order non-Gaussian statistics are more vulnerable to the sampling error due to a limited ensemble size. This paper is organized as follows. Section 2 describes measures for the non-Gaussian PDF. Section 3 describes experimental settings, and Section 4 presents the results. Finally, summary and discussions are provided in Section 5.

84

2 Non-Gaussian measures

Sample skewness $\beta_1^{1/2}$ and sample excess kurtosis β_2 are well-known parametric properties of a non-Gaussian PDF, and are defined as follows:

$$\beta_1^{1/2} = \frac{N}{(N-1)(N-2)} \frac{\sum_{i=1}^N (x_i - \bar{x})^3}{\sigma^3} \quad (1)$$

$$\beta_2 = \frac{N(N+1)}{(N-1)(N-2)(N-3)} \frac{\sum_{i=1}^N (x_i - \bar{x})^4}{\sigma^4} - \frac{3(N-1)^2}{(N-2)(N-3)} \quad (2)$$

where x_i and \bar{x} denote the i th ensemble member and N -member ensemble mean, respectively; σ denotes the sample standard deviation, i.e., $\sigma = \sqrt{\frac{1}{N-1} \sum_{i=1}^N (x_i - \bar{x})^2}$, and skewness $\beta_1^{1/2}$ represents the asymmetry of the PDF. Positive (negative) skewness $\beta_1^{1/2}$ corresponds to the PDF with the longer tail on the right (left) side. Positive (negative) kurtosis β_2 corresponds to the PDF with a more

pointed (rounded) peak and longer (shorter) tails on both sides. When the PDF is Gaussian, both skewness $\beta_1^{1/2}$ and kurtosis β_2 go to zero in the limit of infinite sample size. In addition, we also use Kullback–Leibler divergence (KL divergence, Kullback and Leibler 1951) from the Gaussian PDF. KL divergence is a direct measure of the difference between two PDFs. Let $p(x)$ and $q(x)$ be two PDFs. The KL divergence D_{KL} between the two PDFs is defined as

$$D_{KL} = \int p(x) \log \frac{p(x)}{q(x)} dx \quad (3)$$

Here, we obtain $p(x)$ from the histogram based on the ensemble, and $q(x)$ from the theoretical Gaussian function with the ensemble mean \bar{x} and standard deviation σ , respectively. D_{KL} measures the difference between the ensemble-based histogram and the fitted Gaussian function. Figure 1 shows examples of ensemble-based histograms and corresponding skewness $\beta_1^{1/2}$, kurtosis β_2 , and KL divergence D_{KL} with 10240 samples. Here, the Scott’s choice method (Scott 1979) is applied to decide the bin width for histograms. The histogram with KL divergence $D_{KL} = 0.01$ looks approximately Gaussian while the other three histograms with larger D_{KL} values show significant discrepancies from the Gaussian function. The skewness and kurtosis measure the degrees of symmetry and tailedness, respectively, while the KL divergence D_{KL} is more suitable for measuring the degrees of difference between a given PDF and the fitted Gaussian function. Based on the subjective observation of Fig. 1, hereafter, the PDF is considered to be non-Gaussian when $D_{KL} > 0.01$.

A non-Gaussian PDF can also be caused by outliers. Although detailed results are shown in Section 4, one or several ensemble members are detached from the main cluster; this also results in

the large KL divergence D_{KL} , as well as large skewness and kurtosis, shown in Fig. 2b. We tested two outlier detection methods: the standard deviation-based method (SD method) and the local outlier factor method (LOF method; Breunig et al. 2000). Here, univariate PDFs are considered, so that SD and LOF methods are computed for each variable at each grid point separately.

In the SD method, the ensemble members beyond a prescribed threshold in the unit of SD are defined as outliers. If we make 10240 independent random draws from a Gaussian PDF, statistically 27.6, 0.65, and 0.0059 samples (0.270, 0.00633, and 0.0000573 %) are expected beyond the $\pm 3\sigma$, $\pm 4\sigma$, and $\pm 5\sigma$ thresholds, respectively. Namely, with the threshold of $\pm 3\sigma$, we would expect to detect 27.6 outliers at every grid point. With the $\pm 4\sigma$ threshold, we would expect to detect 1.3 outliers in two grid points (20480 random draws). With the $\pm 5\sigma$ threshold, we would expect to detect 1.18 outliers in 200 grid points (2048000 random draws). Since outliers appear frequently with $\pm 3\sigma$ and $\pm 4\sigma$ thresholds, we choose the $\pm 5\sigma$ threshold for the SD method in this study.

Unlike the SD method, the LOF method is based on the local density, not on the distance from the sample mean. For a given two-dimensional dataset D , let $d(p, o)$ denote the distance between two objects $p \in D$ and $o \in D$. For any positive integer k , define k -distance(p) to be the distance between the object p and the k th nearest neighbor. The k -distance neighborhood of p , or simply $N_k(p)$, is defined as the k nearest objects:

$$N_k(p) = \{q \in D \mid q \neq p, d(p, q) \leq k\text{-distance}(p)\} \quad (4)$$

The cardinality of $N_k(p)$, or $|N_k(p)|$, is greater than or equal to the number of objects (except for the object p itself) within k -distance(p). We define the *reachability distance* of p with respect to the object

130 o as

$$reach-dist_k(p, o) = \max\{k-distance(o), d(p, o)\} \quad (5)$$

131 That is, if the object p is sufficiently distant from the object o , $reach-dist_k(p, o)$ is $d(p, o)$. If they are
 132 sufficiently close to each other, $reach-dist_k(p, o)$ is replaced by $k-distance(o)$ instead of $d(p, o)$. Figure
 133 3 shows a schematic diagram of $reach-dist_k(p, o)$ with $k = 3$. $N_k(p)$ includes o_1, o_2, o_3 , and o_4 , and
 134 $|N_k(p)|$ is 4. In Fig. 3 (a), $reach-dist_k(p, o_1)$ is $k-distance(o_1) = d(o_1, o_4)$ because $k-distance(o_1)$ is
 135 greater than $d(p, o_1)$. In contrast, in Fig. 3 (b), $reach-dist_k(p, o_1)$ is $d(p, o_1)$. We further define the *local*
 136 *reachability density* of p , or simply $lrd_k(p)$, as the inverse of the average of *reachability distance* of
 137 p :

$$lrd_k(p) = \frac{|N_k(p)|}{\sum_{o \in N_k(p)} reach-dist_k(p, o)} \quad (6)$$

139 Finally, the *local outlier factor* of p , denoted as $LOF_k(p)$, is defined as:

$$LOF_k(p) = \frac{\sum_{o \in N_k(p)} \frac{lrd_k(o)}{lrd_k(p)}}{|N_k(p)|}. \quad (7)$$

141 Given a lower *local reachability density* of p and a higher *local reachability density* of p 's k -nearest
 142 neighbors, $LOF_k(p)$ becomes higher. $LOF_k(p)$ or simply LOF is approximately 1 for an object deep
 143 within a cluster, and LOF becomes larger around the edge of the cluster due to sparse objects on the
 144 far side from the cluster. To summarize, the LOF method focuses on the local densities of objects,
 145 and outliers are detected by comparing the local densities. For instance, when $k = 3$ in Fig. 3a, the
 146 local densities of the objects p and $o_{1,2,3,4,5}$ have all similar values because the $k-distance(p)$ is similar
 147 to the $k-distances(o_{1,2,3,4,5})$. Therefore, they are not identified as outliers. In contrast, in Fig. 3b the

148 object p has a smaller local density than the other objects $o_1, 2, 3, 4, 5$ because $k\text{-distance}(p) > k\text{-}$
 149 $\text{distances}(o_1, 2, 3, 4, 5)$. Therefore, the object p has a larger LOF and is identified as an outlier. An object
 150 with LOF much larger than 1 may be categorized as an outlier, but it is not clear how to determine
 151 the threshold for outliers because the threshold also depends on the dataset. The threshold of LOF is
 152 chosen to be 8.0 in this study, and Section 4 shows the results with different values of the threshold
 153 and discusses why we choose this value. k is a control parameter for the LOF method and depends on
 154 the dataset, as shown by Breunig et al. (2000), who suggested that choosing k from 10 to 20 work
 155 well for most of the datasets. If we choose k too small, some objects deeply inside a cluster have a
 156 large LOF , and the LOF method does not work. In fact, using the dataset of KM16, $k = 10$ showed
 157 this problem, while $k = 20$ did not. Therefore, we chose $k = 20$ in this study. Similar to the SD method,
 158 the LOF method is applied to a one-dimensional dataset consisted of 10240 ensemble members.

159 The statistics of the KL divergence, SD and LOF methods with 10240 samples are evaluated
 160 numerically with 1 million trials of 10240 random draws from the standard normal distribution by
 161 the Box-Muller's method (Box and Muller 1958). The results show that the expected value of KL
 162 divergence D_{KL} is 0.0025, and its standard deviation is 0.00048. As for outlier detections, 5767 and
 163 16088 trials have at least one outlier for SD and LOF methods, respectively. Namely, the probabilities
 164 to detect at least one outlier at a grid point are 0.58 % for the SD method and 1.6 % for the LOF
 165 method. Here, the threshold for the SD method is $\pm 5\sigma$. For the LOF method, we choose $k = 20$ and,
 166 as discussed below in Section 4, the threshold value $LOF = 8.0$.

167

168 **3 Experimental settings**

169 We use the 10240-member global atmospheric analysis data from an idealized LETKF experiment of
170 KM16. That is, the experiment was performed with the SPEEDY-LETKF system (Miyoshi 2005)
171 consisting of the SPEEDY model (Molteni 2003) and the LETKF (Hunt et al. 2007; Miyoshi and
172 Yamane 2007). The SPEEDY model is an intermediate AGCM based on the primitive equations at
173 T30/L7 resolution, which corresponds horizontally to 96×48 grid points and vertically to seven
174 levels, and has simplified forms of physical parametrization schemes including large-scale
175 condensation, cumulus convection (Tiedtke 1993), clouds, short- and long-wave radiation, surface
176 fluxes, and vertical diffusion. Due to the very low computational cost, the SPEEDY model has been
177 used in many studies on data assimilation (e.g., Miyoshi 2005; Greybush et al. 2011; Miyoshi 2011;
178 Amezcua et al. 2012; Miyoshi and Kondo 2013; Kondo et al. 2013; MKI14; KM16).

179 The LETKF applies the ETKF (Bishop et al. 2001) algorithm to the local ensemble Kalman filter
180 (LEKF; Ott et al. 2004). The LETKF can assimilate observations at every grid point independently,
181 which is particularly advantageous in high-performance computation. In fact, Miyoshi and Yamane
182 (2007) showed that the parallelization ratio reached 99.99% on the Japanese Earth Simulator
183 supercomputer, and KM16 performed 10240-member SPEEDY-LETKF experiments within 5
184 minutes for one execution of LETKF, not including the forecast part on 4608 nodes of the Japanese
185 K supercomputer. The LETKF is computed as follows. Let \mathbf{X} ($\delta\mathbf{X}$) denote an $n \times m$ matrix, whose
186 columns are composed of m ensemble members (deviations from the mean of the ensemble) with the
187 system dimension n . The superscripts a and f denote the analysis and forecast, respectively. The

188 analysis ensemble \mathbf{X}^a is written as:

$$\mathbf{X}^a = \bar{\mathbf{x}}^f \mathbf{1} + \delta \mathbf{X}^f \left[\tilde{\mathbf{P}}^a (\mathbf{H} \delta \mathbf{X}^f)^T \mathbf{R}^{-1} (\mathbf{y}^o - \mathbf{H} \bar{\mathbf{x}}^f) \mathbf{1} + \sqrt{m-1} (\tilde{\mathbf{P}}^a)^{1/2} \right] \quad (8)$$

189 [cf. Eqs. (6) and (7) of Miyoshi and Yamane 2007]. Here, $\bar{\mathbf{x}}^f$, \mathbf{y}^o , \mathbf{H} , and \mathbf{R} denote the background
 190 ensemble mean, observations, linear observation operator, and observation error covariance matrix,
 191 respectively. $\mathbf{1}$ is an m -dimensional row vector with all elements being 1. The $m \times m$ analysis error
 192 covariance matrix $\tilde{\mathbf{P}}^a$ in the ensemble space is given as

$$\tilde{\mathbf{P}}^a = [(m-1)\mathbf{I}/\rho + (\mathbf{H} \delta \mathbf{X}^f)^T \mathbf{R}^{-1} (\mathbf{H} \delta \mathbf{X}^f)]^{-1} = \mathbf{U} \mathbf{D}^{-1} \mathbf{U}^T \quad (9)$$

193 [cf. Eqs. (3) and (9) of Miyoshi and Yamane 2007]. Here, ρ denotes the covariance inflation factor.
 194 As $\tilde{\mathbf{P}}^a$ is real symmetric, \mathbf{U} is composed of the orthonormal eigenvectors, such that $\mathbf{U} \mathbf{U}^T = \mathbf{I}$. The
 195 diagonal matrix \mathbf{D} is composed of the non-negative eigenvalues.

196 KM16 performed a perfect-model twin experiment for 60 days from 0000 UTC 1 January in the
 197 second year of the nature run, which was initiated at 0000 UTC 1 January from the standard
 198 atmosphere at rest (zero wind). The first year of the nature run was discarded as spin-up. To resolve
 199 detailed PDF structures, the ensemble size was fixed to 10240. No localization was applied, yielding
 200 the best analysis accuracy as shown by KM16 who compared five 10240-member experiments with
 201 different choices of localization: step functions with 2000-km, 4000-km and 7303-km localization
 202 radii, a Gaussian function with a 7303-km localization radius, and no localization. The observations
 203 for horizontal wind components (U, V), temperature (T), specific humidity (Q), and surface pressure
 204 (Ps) were simulated by adding observational errors to the nature run every 6 h at radiosonde-like
 205 locations (cf. Fig. 8, crosses) for all seven vertical levels, but the observations of specific humidity

206 were simulated from the bottom to the fourth model level (about 500 hPa). The observational errors
207 were generated from independent Gaussian random numbers, and the observational error standard
208 deviations were fixed at 1.0 m s^{-1} , 1.0 K , 0.1 g kg^{-1} , and 1.0 hPa for U/V, T, Q, and Ps, respectively.

209 The non-Gaussian measures, skewness $\beta_1^{1/2}$, kurtosis β_2 , and KL divergence D_{KL} , are calculated
210 at each grid point for each variable. Outliers are diagnosed similarly at each grid point for each
211 variable with the SD method and LOF method.

212

213 4 Results

214 Figure 4 shows the spatial distributions of the analysis absolute error, ensemble spread, background
215 skewness $\beta_1^{1/2}$, kurtosis β_2 , and KL divergence D_{KL} for temperature at the fourth model level (~500
216 hPa) at 0600 UTC 22 February. When the analysis absolute error is large, the background non-
217 Gaussian measures also tend to be large, especially in the tropics. The peaks for skewness $\beta_1^{1/2}$,
218 kurtosis β_2 , and KL divergence D_{KL} tend to coincide. Although grid point A (16.7°S , 90.0°E) has a
219 large KL divergence D_{KL} with large analysis absolute error, at grid point B (35.3°N , 146.3°E) with a
220 large KL divergence D_{KL} the analysis absolute error is small ($< 0.08 \text{ K}$). This result shows that the
221 large analysis error is not always associated with the strong non-Gaussianity at a specific time. The
222 PDFs at grid points A and B are shown in Fig. 2a, b, respectively. The histogram at the grid point A
223 is clearly a multimodal PDF with KL divergence $D_{KL} > 0.01$, and the right mode captures the truth
224 (yellow star). At grid point B, although the PDF seems to be closer to Gaussian, skewness $\beta_1^{1/2}$ and

225 kurtosis β_2 are much larger than those at grid point A. In fact, the PDF does not fit to the Gaussian
 226 function calculated by the ensemble mean and standard deviation. Zooming in on the left side of Fig.
 227 2b shows a small cluster composed of 76 members detached from the main cluster; 74 members of
 228 the small cluster exceed -5σ and are categorized as outliers in the SD method. This small cluster
 229 causes the standard deviation to become large and results in the Gaussian function having a longer
 230 tail than the histogram. The small cluster should not be considered as consisting of outliers because
 231 it may have some physical significance. Scatter diagrams of *LOF* versus distance from ensemble
 232 mean for all ensemble members at grid points A and B are shown in Fig. 5a, b, respectively. At grid
 233 point A, *LOF* is not so large even at the edge of the cluster (< 4), and the multimodal PDF does not
 234 influence *LOF*. In addition, all members are within $\pm 3\sigma$. Therefore, there are no clear outliers at grid
 235 point A. At grid point B, although most of the small cluster exceeds -5σ , the maximum *LOF* in the
 236 small cluster is still smaller than 3. This indicates that all members of the small cluster should not be
 237 outliers in the LOF method. As an outlier case, we pick up the grid point C (35.3°N, 112.5°W) in Fig.
 238 4. The PDF at the grid point C fits the Gaussian function well, and the non-Gaussian measures are
 239 quite small (Fig. 2c). A member on the left edge of the scatter diagram in Fig. 5c has the largest *LOF*
 240 > 8.0 , but the member is within $\pm 3\sigma$. As mentioned in Section 2, the threshold of *LOF* for outliers
 241 depends on the dataset. Figure 6 shows the number of outliers for thresholds of 5.0, 8.0, and 11.0 at
 242 0600 UTC 22 February. There are too many outliers with threshold = 5.0, but in contrast, the number
 243 of outliers decreases markedly with threshold = 8.0 or 11.0. Based on these results, and as already
 244 mentioned in Section 2, we adopt $LOF = 8.0$ as a threshold for outliers.

245 Figure 7 shows the spatial distributions of the time-mean analysis RMSE, ensemble spread, the
 246 background absolute skewness $\beta_1^{1/2}$, absolute kurtosis β_2 , and KL divergence D_{KL} . As mentioned in
 247 KM16, the time-mean ensemble spread corresponds well to the RMSE, which is larger in the tropics.
 248 The pattern correlation between the RMSE and ensemble spread is 0.97. Moreover, the distributions
 249 of non-Gaussian measures are similar to each other and also correspond well to the RMSE and
 250 ensemble spread. The RMSE and non-Gaussian measures differ in that the non-Gaussianity is large
 251 in storm tracks, such as the North Pacific Ocean and the North Atlantic Ocean. This may be because
 252 the LETKF inhibits growing errors well in storm tracks regardless of the strong non-Gaussianity. To
 253 investigate the non-Gaussianity in more detail, Figs. 8 and 9 show the frequencies of non-Gaussian
 254 PDF with high KL divergence $D_{KL} > 0.01$ and identifying at least one outlier with high $LOF > 8.0$
 255 on a 10240-member ensemble, respectively. The frequency of non-Gaussian PDF is defined as the
 256 ratio of non-Gaussianity appearance at every grid point during the 36-day period from 0000 UTC 25
 257 January to 1800 UTC 1 March. The spatial distribution of frequency of non-Gaussianity for
 258 temperature is similar to that of the time mean RMSE and D_{KL} (Figs. 7 a, e, and 8 b), and the pattern
 259 correlation between the spatial distribution of mean RMSE and D_{KL} is 0.68. We find high frequency
 260 of non-Gaussian PDF in the tropics and storm track regions for temperature, specific humidity, and
 261 surface pressure, although non-Gaussian PDF seldom appears in the densely observed regions. In the
 262 tropics, the frequency reaches up to 90%, and in South America the frequency reaches the highest
 263 value over 95%, i.e., the non-Gaussian PDF appears for 34 days out of 36 days. In contrast, the non-
 264 Gaussian PDF for zonal wind hardly appears (Fig. 8 a), and the intensity of the non-Gaussianity, as

265 evaluated by other measures, is also weak (not shown). On the other hand, the outliers appear almost
266 randomly and do not clearly depend on the region for any of the variables (Fig. 9), and most outliers
267 disappear within only one or a few analysis steps. Moreover, there are no correlations between the
268 frequency of outliers and analysis RMSE.

269 To investigate how the non-Gaussian PDF is generated, we plot the forecast and analysis update
270 processes at 1.9°N, 168.7°E for 256 members chosen randomly from 10240 members from the
271 analysis at 0000 UTC 9 February (157th analysis cycle) to the forecast at 0000 UTC 10 February
272 (161st analysis cycle, Fig. 10a). That is, Fig. 10a shows the lifecycle of the non-Gaussian PDF. As the
273 vertical axis, we introduce the convective instability $d\theta_e$, which is defined as a difference between
274 equivalent potential temperature θ_e at the fourth model level (~500 hPa) and θ_e at the second model
275 level (~850 hPa). Negative (Positive) $d\theta_e$ indicates a convectively unstable (stable) atmosphere. The
276 non-Gaussian PDF appears in the background at the 159th cycle (1200 UTC 9 February), and the
277 model forecast increases the KL divergence D_{KL} for $d\theta_e$ up to 0.154 with a bimodal PDF of clusters
278 A and B. We find many lines crossing in the forecast step from the analyses at the 158th cycle to the
279 background at the 159th cycle. Namely, many of the upper side cluster A at the 159th cycle come from
280 the lower side analyses in the previous 158th cycle, generally reducing the instability (increasing
281 values of $d\theta_e$) in the forecast step, and vice versa for the lower side cluster B. In the background
282 temperature at the fourth model level, the KL divergence D_{KL} also increases from 0.003 to 0.299 for
283 6 h (Figs. 10b, c). Finally, the non-Gaussian PDF almost disappears at the 161st cycle (0000 UTC 10
284 February). Figure 11 shows a scatter diagram of 0600 UTC versus 1200 UTC 9 February for

285 background temperature in the fourth model level for each member at 1.9°N, 168.7° E, and also shows
 286 histograms corresponding to the scatter diagrams. The PDF at 0600 UTC is almost Gaussian.
 287 However, at 1200 UTC, the bimodal structure with KL divergence $D_{KL} = 0.299$ appears. The dot
 288 colors show $d\theta'_e$ evaluated from 0600 UTC to 1200 UTC 9 February, namely, $d\theta'_e =$
 289 $(d\theta_{e\ 1200\ UTC} - d\theta_{e\ 0600\ UTC}) - (d\bar{\theta}_{e\ 1200\ UTC} - d\bar{\theta}_{e\ 0600\ UTC})$, where $\bar{\theta}_e$ indicates the equivalent
 290 potential temperature calculated from the ensemble mean. That is, a red (blue) dot shows more
 291 stability (instability) than the ensemble mean. The red and blue dots are clearly divided into the right
 292 and left side modes, respectively. Most members with mitigated (enhanced) instability move to the
 293 right (left) side mode. The members with larger (smaller) temperature values at 1200 UTC correspond
 294 to larger (smaller) values of stability as shown by the warmer (colder) color. In addition, both right
 295 and left modes correspond to the opposite side modes in the specific humidity, respectively (not
 296 shown). That is, the members with higher (lower) temperature have lower (higher) humidity than the
 297 ensemble mean. The instability is driven by precipitation. Figure 12 is similar to Fig. 11, but for
 298 precipitation. The 10240 members are clearly divided into three clusters at 1200 UTC by the
 299 instability. The three clusters indicate the number of times cumulus parameterization is triggered.
 300 Most members in the right (left) cluster are red (blue) and show mitigation (enhancement) of the
 301 instability. Figure 13 is also similar to Fig. 11, but for zonal wind at the fourth model level. In
 302 agreement with what has been seen on Fig. 8a, the non-Gaussianity of zonal wind is weak, and the
 303 bimodal structure appearing in temperature and humidity seldom affects the PDF of zonal wind. We
 304 found no relationship between the atmospheric instability and zonal wind. Therefore, the genesis of

non-Gaussian PDF in the tropics is deeply related to precipitation process, which is driven by convective instability through cumulus parameterization in the SPEEDY model. As a result, the precipitation process mitigates the instability, with rising temperature and decreasing humidity. Similar results are generally obtained at other grid points with non-Gaussian PDF.

In the extratropics, non-Gaussian PDF is generated differently. To investigate the genesis of non-Gaussian PDF in the extratropics, we focus on a case around an extratropical cyclone over the Atlantic Ocean. A non-Gaussian PDF appears at 0600 UTC 15 February at 42.7°N, 48.8°W, and the KL divergence D_{KL} of background temperature increases from 0.003 to 0.460 (Fig. 14, crosses). Figure 15 is similar to Fig. 11, but for background specific humidity at the second model level (~850 hPa) versus precipitation at 42.7°N, 48.8°W at 0006 UTC 15 February. Trimodal PDFs appear in both specific humidity and precipitation. The three modes of specific humidity are clearly separated by the color, i.e., instability $d\theta'_e$. Namely, modes with larger humidity has colder colors (smaller $d\theta'_e$ corresponding to more instability). However, the three modes of precipitation show no clear dependence on $d\theta'_e$. Therefore, the trimodal PDF of specific humidity would not be driven by the cumulus parameterization. Next, the relationship between background specific humidity and meridional wind at the second model level (~850 hPa) is shown in Fig. 16. The members in the left mode have lower specific humidity with relatively stronger northerly wind. If we look at the fourth model level (~500 hPa) for these members with lower humidity, they have relatively weaker northerly wind and warm temperature (not shown). Namely, instabilities are mitigated by the northerly advection of dry air at the lower troposphere and by warm temperature at the mid troposphere. In this

case study, the non-Gaussianity genesis in the extratropics is associated with the advections. This is
 only an example, and the non-Gaussianity genesis in the extratropics is generally more complicated
 and would be affected by not only vertical stratification but also larger-scale atmospheric phenomena
 such as extratropical cyclones and advections. Here, we do not go into details for different cases of
 non-Gaussianity genesis, but instead, this is further discussed in Section 5.

The non-Gaussian measures are sensitive to the ensemble size due to sampling errors. Figure 17
 shows the spatial distributions of the skewness $\beta_1^{1/2}$, kurtosis β_2 , and KL divergence D_{KL} for
 temperature at the fourth model level (~ 500 hPa) at 0600 UTC 22 February with 80, 320, and 1280
 subsamples from 10240 members, respectively. Skewness $\beta_1^{1/2}$, kurtosis β_2 , and KL divergence D_{KL}
 with 80 members contain high levels of contaminating errors originating from sampling errors, and
 the non-Gaussian measures are difficult to distinguish from the contaminating errors. With increasing
 the ensemble size up to 1280, the sampling errors become smaller by gradation. With 1280 members,
 the sampling errors are essentially removed, and the distributions are comparable to those with 10240
 members (see Fig. 4). Therefore, a sample size of about 1000 members is necessary to represent non-
 Gaussian PDF. The outliers also depend on the sample size. Figure 18 shows LOF with 80, 320, 1280,
 and 5120 subsamples from 10240 members for temperature at the fourth model level at the grid point
 B (35.3°N , 146.3°E), as in Fig. 5b. With 80 members, there are no outliers as the LOF of each member
 is much smaller than the outlier threshold of 8.0. When the ensemble size is 320, four members with
 high $LOF > 8.0$ are identified as outliers. With the ensemble sizes of 1280 and 5120, 13 and 41
 members construct a small cluster, respectively, but they are not outliers with the threshold of $LOF =$

345 8.0. With increasing the ensemble size up to 10240, the *LOFs* of the small cluster and main cluster
346 show almost the same value (Fig. 5b).

347 We saw a good agreement between the RMSE and ensemble spread (Figs. 7a, b), but it is useful
348 to further evaluate the 10240-member ensemble using ranked probability scores. The rank histogram
349 (Hamill and Collucci 1997, Talagrand et al. 1999, Anderson 1996, Hamill 2001) evaluates the
350 reliability of ensemble statistically. Figure 19 shows almost flat rank histograms at all grid points and
351 the grid points with non-Gaussian PDF. The truth is known in this study and used as a verifying
352 analysis. The flat rank histograms correspond to healthy background ensemble distributions. The
353 continuous ranked probability score (CRPS, Hersbach 2000) is another method to evaluate ensemble
354 distributions, decomposed into reliability, resolution and uncertainty as

$$\text{CRPS} = \text{Reli} - \text{Resol} + U. \quad (10)$$

355 Here, the reliability Reli becomes zero under the perfectly reliable system. The resolution Resol
356 indicates the degree to which the ensemble distinguishes situations with different frequencies of
357 occurrence, and is associated with the accuracy or sharpness. The uncertainty U measures the
358 climatological variability. The reliability, resolution and uncertainty are given on the prescribed area
359 as

$$\begin{aligned} \text{Reli} &= \sum_{i=0}^N \bar{g}_i (\bar{o}_i - p_i)^2, \\ p_i &= \frac{i}{N}, \end{aligned} \quad (11)$$

$$U - \text{Resol} = \sum_{i=0}^N \bar{g}_i \bar{o}_i (1 - \bar{o}_i), \quad (12)$$

$$U = \sum_{k,l < k} w_k w_l |y^k - y^l|, \quad (13)$$

360 [cf. Eqs 36, 37 and 19 in Hersbach 2000, respectively]. Here, \bar{g}_i is the area-weighted average width
 361 of the bin i between consecutive ensemble members x_i and x_{i+1} , and \bar{o}_i is the area-weighted average
 362 frequency that the verifying analysis is less than $(x_{i+1} + x_i)/2$. N denotes an ensemble size. In this
 363 study, y^k and y^l indicate the anomalies between the background ensemble mean and monthly
 364 climatology computed from a 30-year nature run at the grid points k and l , respectively. The weights
 365 w_k, w_l are proportional to the cosine of latitude. Table 1 shows that the reliability is closer to zero and
 366 that the resolution is much higher at all grid points than at the grid points with non-Gaussian PDF.
 367 Therefore, the non-Gaussian PDF has a negative impact on updating the state variables for the LETKF.
 368 The smaller uncertainty at the grid points with non-Gaussian PDF reflects generally smaller variations
 369 in the tropics where the non-Gaussian PDFs frequently appear. Similar results are obtained for the
 370 other variables.

371

372 **5 Summary and discussions**

373 Kalman filters provide the minimum variance linear estimator, which coincides with the maximum
 374 likelihood estimator if the PDFs are Gaussian. This study investigated the non-Gaussian PDF and its
 375 behavior using the SPEEDY-LETKF system with 10240 members. Non-Gaussian PDFs appear

376 frequently in the areas where the RMSE and ensemble spread are larger. Moreover, an ensemble size
377 of about 1000 is necessary to identify the possible non-Gaussianity of PDFs, which may be difficult
378 to detect in the presence of sampling error.

379 The non-Gaussian PDF appears frequently in the tropics and the storm track regions over the
380 Pacific and Atlantic Oceans, particularly for temperature and specific humidity, but not for winds.
381 With the SPEEDY model, the genesis of non-Gaussian PDF in the tropics is mainly associated with
382 the convective instability. These results suggest that the non-Gaussianity be mainly caused by
383 precipitation processes such those associated with cumulus convection, but much less by dynamic
384 processes. Generally, the atmosphere in the tropics tends to become unstable, and the convective
385 instability is mitigated by vertical convection with precipitation. In the SPEEDY model, a simplified
386 mass-flux scheme developed by Tiedtke (1993) is applied. Convection occurs when either the specific
387 or relative humidity exceeds a prescribed threshold (Molteni 2003). The members that hit the
388 threshold have precipitation, and this process mitigates their own convective instability resulting in a
389 temperature rise and humidity decrease. In contrast, the members with no or little precipitation
390 enhance or cannot mitigate their own convective instability. Therefore, convective instability is a key
391 to non-Gaussianity genesis in the tropics in the SPEEDY model.

392 In the extratropics, non-Gaussianity is generally weak and seldom appears except in the storm
393 track regions, where the genesis of non-Gaussian PDF is also associated with instabilities, but with
394 different processes from the tropics. This study focused on a case near the extratropical cyclone in
395 the North Atlantic, and the results showed that the instability was associated with the horizontal

396 advections. The members with reduced instabilities had lower humidity at the lower troposphere and
397 higher temperature at the mid troposphere by meridional advections. In contrast, the members with
398 higher humidity at the lower troposphere and lower temperature at the mid troposphere enhanced
399 their instability. Moreover, the precipitation process through the cumulus parameterization did not
400 explain the non-Gaussian PDF. Precipitation associated with extratropical cyclones is usually caused
401 by synoptic-scale baroclinic instabilities and does not mitigate the local instability completely.

402 As mentioned in Section 4, to generalize the process of non-Gaussianity genesis in the extratropics
403 is not simple. The non-Gaussianity genesis is generally associated with instability from various
404 processes such as the convection, advection and larger-scale atmospheric phenomena, so that it is
405 very difficult to find general mechanisms of the non-Gaussianity genesis in the extratropics even for
406 the simple SPEEDY model. Furthermore, if we use more realistic models with complex physics
407 schemes, the process of non-Gaussianity genesis would be much more diverse and complicated. This
408 is partly why we did not go into details to investigate different cases of non-Gaussianity genesis with
409 the SPEEDY model.

410 The non-Gaussianity is less frequent in the wind components not only in the time scale of 1 month
411 but also for the snapshot, although the dynamic process of the atmosphere is a nonlinear system.
412 Moreover, the non-Gaussian PDFs of temperature and specific humidity seldom affect the PDFs of
413 the wind components. We hypothesize that the model complexity may be a reason for this. The
414 SPEEDY model could not resolve some local interactions between wind components and other
415 variables due to its coarse resolution and simplified processes. With more realistic models, physical

416 processes are much more complex, and the local interactions can also be represented. Indeed, we
417 obtained widely distributed non-Gaussianity with a 10240-member NICAM-LETKF system with
418 112-km horizontal resolution assimilating real observations from the National Centers for
419 Environmental Prediction (NCEP) known as PREPBUFR from 0000 UTC 1 November to 0000 UTC
420 8 November (Miyoshi et al. 2015). Figure 20 shows the spatial distributions of background KL
421 divergence of zonal wind and temperature at the second model level (~ 850 hPa) for SPEEDY at 0000
422 UTC 1 March and zonal wind and temperature at the eighth model level (~ 850 hPa) for the NICAM
423 at 0000 UTC 8 November 2011. With NICAM, the non-Gaussianity appears globally not only in the
424 temperature field but also in the zonal wind although we should account for the model errors of
425 NICAM. This result implies that the NICAM has various sources of non-Gaussianity such as smaller
426 scale physical and dynamical processes with various interactions among different model variables,
427 and suggests the limitation of this study using the SPEEDY model. In the realistic situation, we would
428 presumably have more frequent occurrence of non-Gaussianity.

429 The outliers appear almost randomly regardless of locations, levels, and variables, and the lifetime
430 is about a few analysis steps. When the outliers appear, the number of outliers is basically one per
431 grid point, but sometimes the number is more than one. Anderson (2010) also reported similar results
432 using a low-order dry atmospheric model. These results seem not to be consistent with Amezcua et
433 al. (2012) who reported that just one outlier appeared with the ensemble square root filters in low-
434 dimensional models and that the outlier did not rejoin the cluster easily. These properties of their
435 outlier and our outliers in the SPEEDY model are somewhat different. In the low-dimensional models,

436 a certain ensemble member tends to become an outlier at all grid points and all variables. In contrast,
437 the outliers in the SPEEDY model appear at just some grid points but not all grid points and do not
438 appear in all variables simultaneously. In addition, the negative influence of outliers on the analysis
439 accuracy may be sufficiently small in high-dimensional models due to the randomness and short
440 longevity of outliers. In fact, the results showed no clear correspondence between the outlier
441 frequency and analysis accuracy. These are the results from the simple SPEEDY model. It remains to
442 be a subject of future research how the outliers behave with a more realistic model and real
443 observations.

444 As measures of non-Gaussianity, skewness, kurtosis, and KL divergence for the non-Gaussianity,
445 and the SD and LOF methods for outliers, are introduced and compared with each other. The KL
446 divergence is a more suitable measure because it measures the direct difference between the
447 ensemble-based histogram and the fitted Gaussian function. The LOF method is better than the SD
448 method because it can detect the outliers depending on the density of objects. Although it is easy to
449 detect the outliers using the SD method, misdetection of outliers is possible because this method
450 categorizes a small cluster far from the main cluster into outliers. The small cluster may be generated
451 through physical processes and have physical significance; this should not be treated as outliers. The
452 measures of non-Gaussianity are evaluated in the univariate field in this study. An extension to
453 multivariate fields with multivariate analysis remains as a subject of future research.

454 Non-Gaussian measures tend to be more sensitive to the sampling error due to the limited
455 ensemble size (see Figs. 17, 18). When the ensemble size is small, it is difficult to determine whether

456 a split member is a real outlier or a sample from a small cluster. Amezcua et al. (2012) discussed the
457 outliers by skewness using the 20-member SPEEDY-LETKF and reported that the skewness is clearly
458 large in the tropics and the Southern Hemisphere for the temperature and humidity fields. These
459 results were not consistent with those of the present study because the outliers appear randomly.
460 However, this inconsistency may have been due to the small ensemble size. The large skewness of
461 Amezcua et al. (2012) could possibly indicate the non-Gaussianity rather than the outliers with a large
462 ensemble size. Having a sufficient ensemble size, suggested to be about 1000 according to this study,
463 would be essential when discussing about non-Gaussianity and outliers.

464

465 **Data availability**

466 All data and source code are archived in RIKEN Center for Computational Science and are available
467 upon request from the corresponding authors under the license of the original providers. The original
468 source code of the SPEEDY-LETKF is available at <https://github.com/takemasa-miyoshi/letkf>.

469

470 **Acknowledgments**

471 The authors are grateful to the members of the Data Assimilation Research Team, RIKEN R-CCS and
472 of the Meteorological Research Institute for fruitful discussions. The SPEEDY-LETKF code is
473 publicly available at <https://github.com/takemasa-miyoshi/letkf>. Part of the results was obtained using

474 the K computer at the RIKEN R-CCS through proposal numbers ra000015 and hp150019. This study
475 was partly supported by JST CREST Grant number JPMJCR1312, and JSPS KAKENHI Grant
476 number JP16K17806.

477

478

479 **References**

- 480 Anderson, J. L.: A method for producing and evaluating probabilistic forecasts from ensemble
481 model integrations, *J. Climate*, 9, 1518–1530, 1996.
- 482 Anderson, J. L.: An ensemble adjustment Kalman filter for data assimilation, *Mon. Wea. Rev.*, 129,
483 2884-2903, 2001.
- 484 Anderson, J. L.: A non-Gaussian ensemble filter update for data assimilation, *Mon. Wea. Rev.*, 138,
485 4186-4198, 2010.
- 486 Amezcu, J., Ide, K., Bishop, C. H., and Kalnay, E.: Ensemble clustering in deterministic ensemble
487 Kalman filters, *Tellus*, 64A, 1-12, 2012.
- 488 Bishop, C. H., Etherton, B. J. and Majumdar, S. J.: Adaptive sampling with the ensemble transform
489 Kalman filter. Part I: Theoretical aspects. *Mon. Wea. Rev.*, 129, 420-436, 2001.
- 490 Box, G. E. P. and Muller, Mervin E.: A note on the generation of random normal deviates, *Ann.*
491 *Math. Statist.*, 29, 610-611, doi:10.1214/aoms/1177706645.
- 492 Breunig, M. M, Kriegel, H. P. R., Ng, T., and Sander, J.: LOF: Identifying density-based local
493 outliers, *Proceedings of the 2000 ACM SIGMOD International Conference on Management of*
494 *Data*, 93-104, doi: 10.1145/335191.335388, 2000.
- 495 Evensen, G.: Sequential data assimilation with a nonlinear quasi-geostrophic model using Monte
496 Carlo methods to forecast error statistics, *J. Geophys. Res.* 99C5, 10143-10162, 1994.
- 497 Greybush, S. J., Kalnay, E., Miyoshi, T., Ide, K., and Hunt, B. R.: Balance and ensemble Kalman
498 filter localization techniques, *Mon. Wea. Rev.*, 139, 511-522, 2011.

499 Hamill, T. M.: Interpretation of rank histograms for verifying ensemble forecasts, Mon. Wea. Rev.,
500 129, 550-560, 2001.

501 Hamill, T., and Colucci, S. J.: Verification of Eta–RSM short- range ensemble forecasts, Mon. Wea.
502 Rev., 125, 1312–1327, 1997.

503 Hersbach, H.: Decomposition on the continuous ranked prob- ability score for ensemble prediction
504 systems, Wea. Forecasting, 15, 559–570, 2000.

505 Hunt, B. R., Kostelich, E. J., and Syzunogh, I.: Efficient data assimilation for spatiotemporal chaos:
506 A local ensemble transform Kalman filter, Physica D, 230, 112-126, 2007.

507 Kalman, R. E.: A new approach to linear filtering and predicted problems, J. Basic Eng.. 82, 35-45,
508 1960.

509 Kondo, K. and Miyoshi, T.: Impact of removing covariance localization in an ensemble Kalman
510 filter: experiments with 10240 members using an intermediate AGCM, Mon. Wea. Rev., 144,
511 4849-4865, 2016.

512 Kondo, K. and Miyoshi, T., and Tanaka, H. L.: Parameter sensitivities of the dual-localization
513 approach in the local ensemble transform Kalman filter, SOLA, 9, 174-178, 2013.

514 Kullback, S., and Leibler, R. A.: On information and sufficiency, The Annals of Mathematical
515 Statistics, 22, 79-86, 1951.

516 Miyoshi, T.: *Ensemble Kalman Filter Experiments with a Primitive-equation Global Model*. PhD
517 Thesis, University of Maryland, College Park, 226 pp., 2005.

518 Miyoshi, T.: The Gaussian approach to adaptive covariance inflation and its implementation with

519 the local ensemble transform Kalman filter, *Mon. Wea. Rev.*, 139, 1519–1535, doi:
520 10.1175/2010MWR3570.1, 2011.

521 Miyoshi, T. and Yamane, S.: Local ensemble transform Kalman filtering with an AGCM at a
522 T159/L48 resolution, *Mon. Wea. Rev.*, 135, 2841–3861, 2007.

523 Miyoshi, T. and Kondo, K.: A multi-scale localization approach to an ensemble Kalman filter,
524 *SOLA*, 9, 170–173, 2013.

525 Miyoshi, T., Kondo, K., and Imamura, T.: 10240-member ensemble Kalman filtering with an
526 intermediate AGCM. *Geophys. Res. Lett.*, 41, 5264–5271, doi: 10.1002/2014GL060863, 2014.

527 Miyoshi, T., Kondo, K., and Terasaki, K.: Big Ensemble Data Assimilation in Numerical Weather
528 Prediction, *Computer*, 48, 15–21, doi:10.1109/MC.2015.332, 2015.

529 Molteni, F.: Atmospheric simulations using a GCM with simplified physical parameterizations. I:
530 model climatology and variability in multi-decadal experiments, *Clim. Dyn.*, 20, 175–191, 2003.

531 Ott, E., and Coauthors: A local ensemble Kalman filter for atmospheric data assimilation, *Tellus*, 56A,
532 415–428, 2004.

533 Pearson, Egon S.: Note on tests for normality, *Biometrika*, 22, 423–424, 1931.

534 Posselt, D., and Bishop, C. H.: Nonlinear parameter estimation: comparison of an ensemble Kalman
535 smoother with a Markov chain Monte Carlo algorithm, *Mon. Wea. Rev.*, 140, 1957–1974,
536 2012.

537 Satoh, M., Matsuno, T., Tomita, H., Miura, H., Nasuno, T., and Iga, S.: Nonhydrostatic icosahedral
538 atmospheric model (NICAM) for global cloud resolving simulations, *Journal of Computational*

539 Physics, the special issue on Predicting Weather, Climate and Extreme events, 227, 3486-3514,
540 doi:10.1016/j.jcp.2007.02.006, 2008.

541 Satoh, M., Tomita, H., Yashiro, H., Miura, H., Kodama, C., Seiki, T., Noda, A. T., Yamada, Y., Goto,
542 D., Sawada, M., Miyoshi, T., Niwa, Y., Hara, M., Ohno, T., Iga, S., Arakawa, T., Inoue, T., and
543 Kubokawa, H.: The non-hydrostatic icosahedral atmospheric model: Description and
544 development, Progress in Earth and Planetary Science, 1, 18, doi:10.1186/s40645-014-0018-1,
545 2014.

546 Scott, D. W.: On optimal and data-based histograms, Biometrika, 66, 605-610,
547 doi:10.1093/biomet/66.3.605, 1979.

548 Talagrand, O., Vautard, R., and Strauss, B.: Evaluation of Probabilistic Prediction Systems,
549 Proceedings of Workshop on *Predictability*, European Centre for Medium-range Weather
550 Forecasts, Reading, England, October 1997, 1-25, 1999.

551 Tiedtke, M: A comprehensive mass flux scheme for cumulus parameterization in large-scale
552 models, Mon. Wea. Rev., 117, 1779-1800, 1993.

553 Tomita, H., and Satoh, M.: A new dynamical framework of nonhydrostatic global model using the
554 icosahedral grid, Fluid Dyn. Res., 34, 357-400, 2004.

555

556

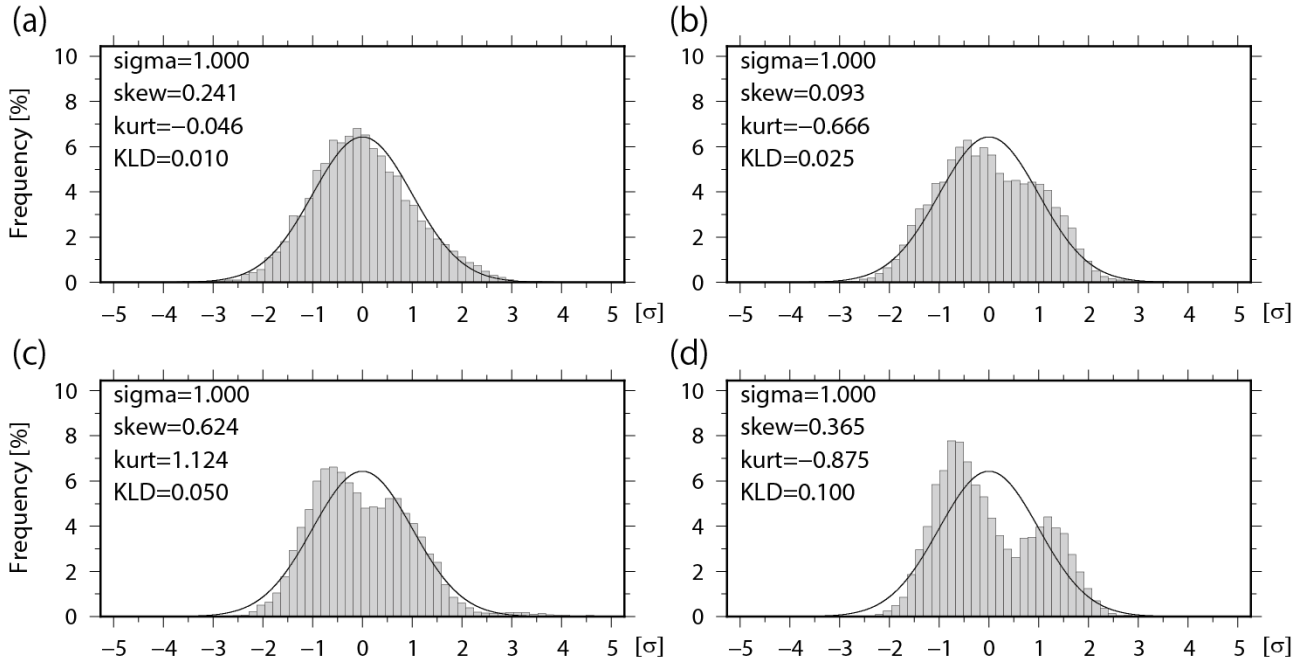


Figure 1: Ensemble-based histograms with 10240 ensemble members when the Kullback–Leibler (KL) divergence D_{KL} = (a) 0.010, (b) 0.025, (c) 0.050, and (d) 0.100. Solid lines indicate fitted Gaussian functions. Skewness (skew) and kurtosis (kurt) are also shown in the figure.

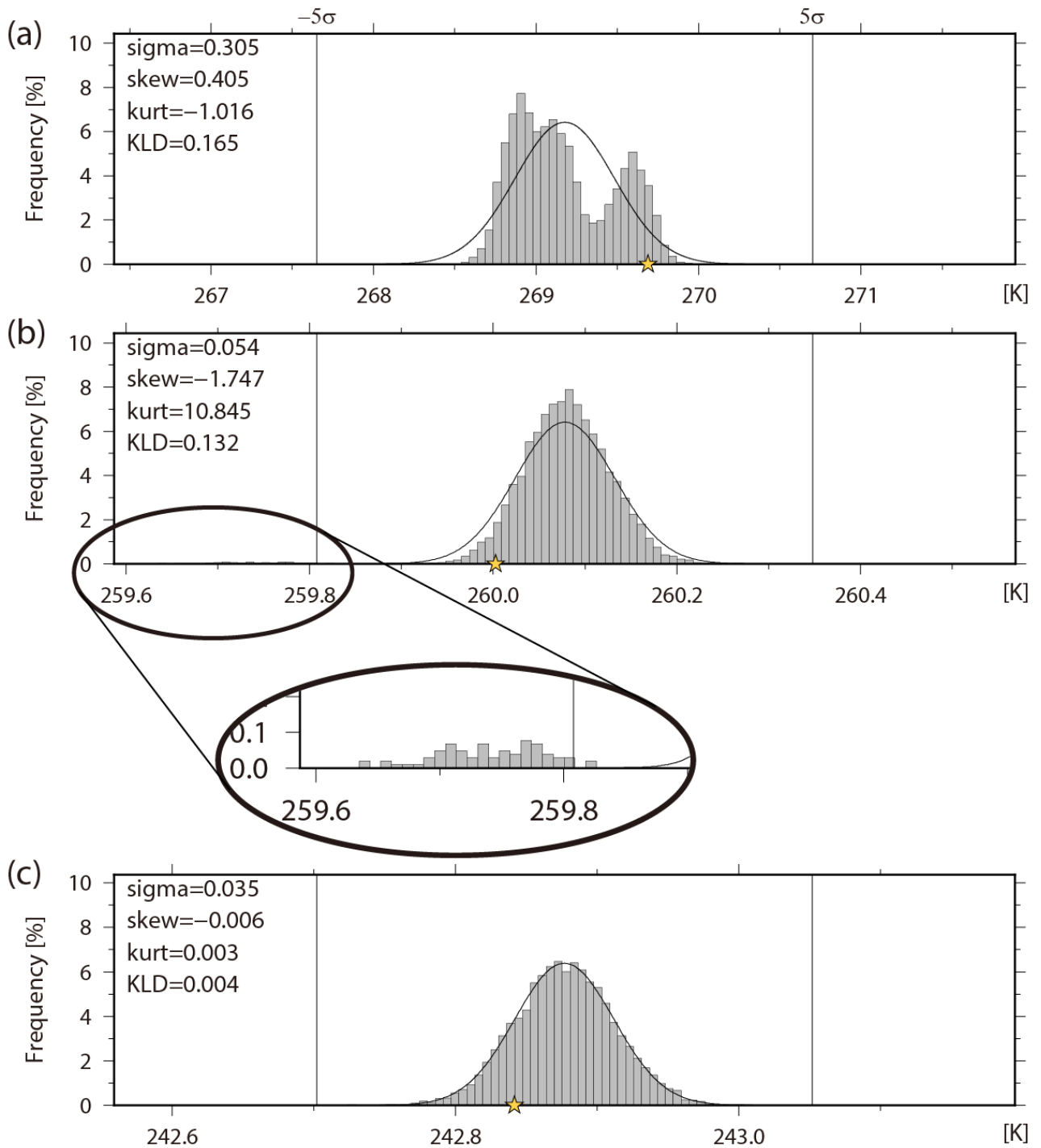
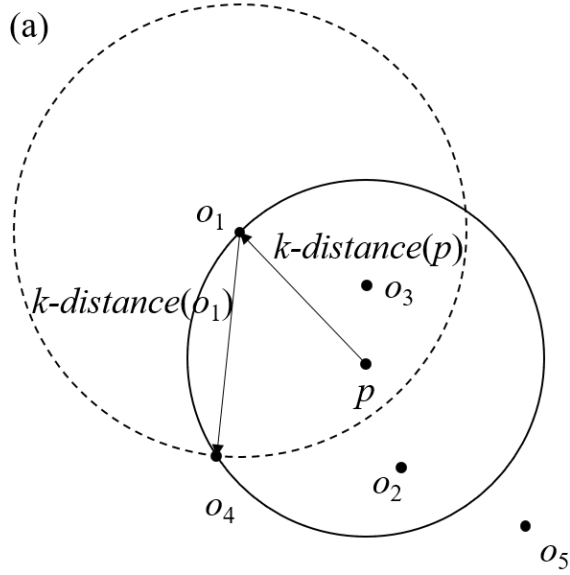
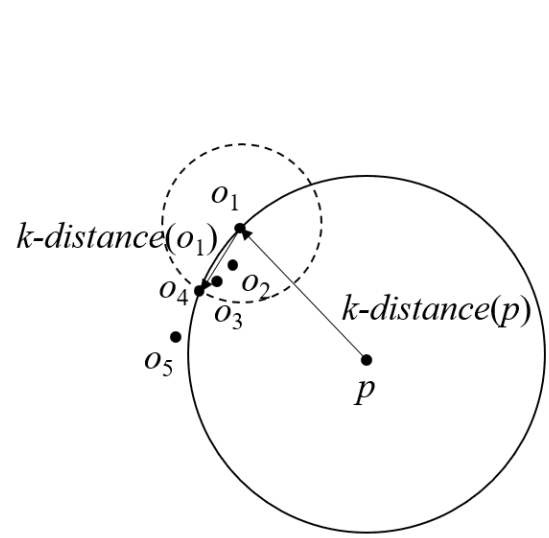


Figure 2: Histograms of background temperature (K) at the fourth model level (~500 hPa) at (a) grid point A (16.7°S, 90.0°E), (b) grid point B (35.3°N, 146.3°E), and (c) grid point C (35.3°N, 112.5°W). The yellow star shows the truth.



$$\begin{aligned}
 \text{reach-dist}_k(p, o_1) &= \max \{k\text{-distance}(o_1), d(p, o_1)\} \\
 &= k\text{-distance}(o_1) \\
 &= d(o_1, o_4)
 \end{aligned}$$



$$\begin{aligned}
 \text{reach-dist}_k(p, o_1) &= \max \{k\text{-distance}(o_1), d(p, o_1)\} \\
 &= \max \{k\text{-distance}(o_1), d(p, o_1)\} \\
 &= d(p, o_1)
 \end{aligned}$$

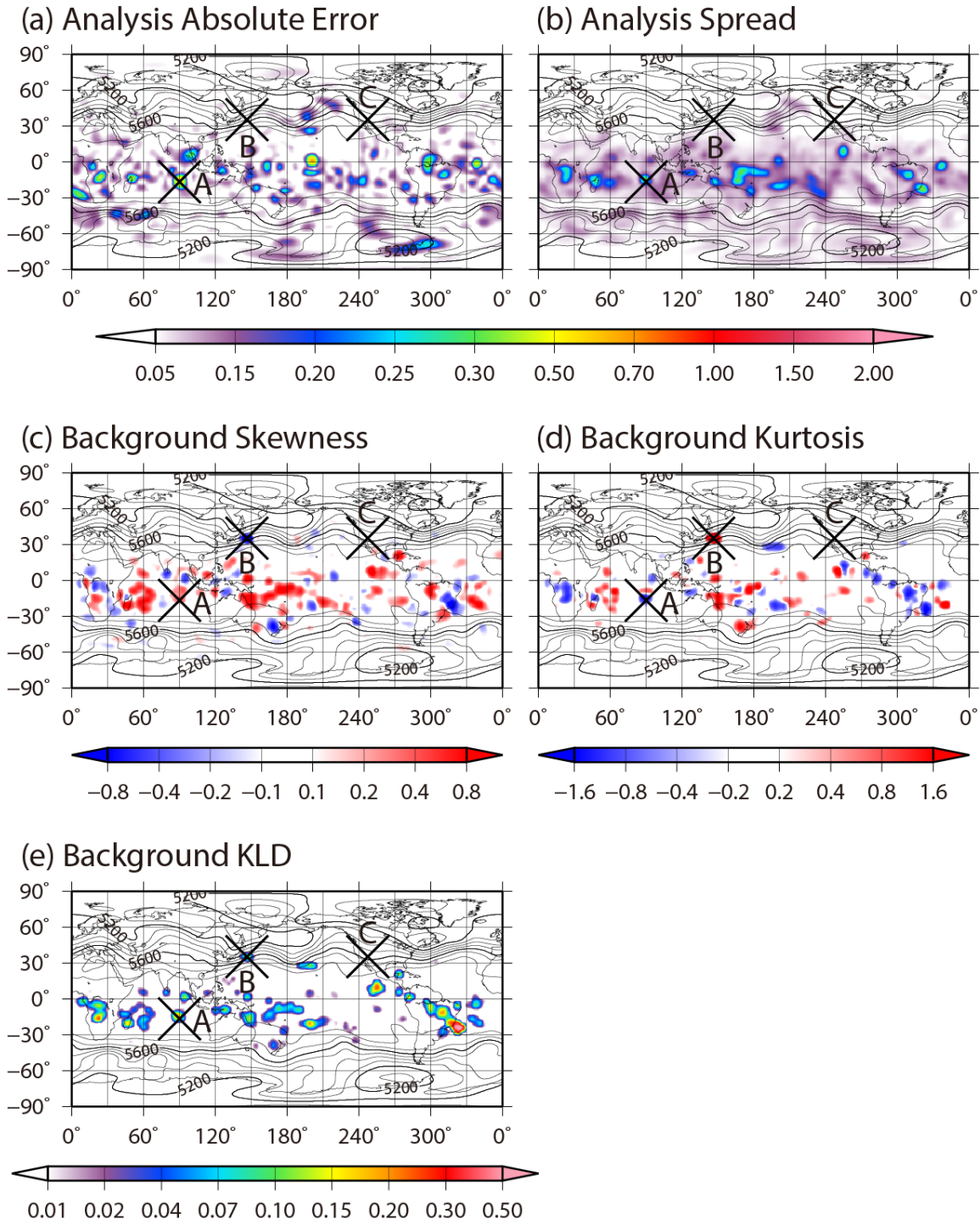
567

568 Figure 3: Schematic diagrams of $\text{reach-dist}_k(p, o)$ with $k = 3$ for (a) uniformly distributed data and

569 (b) data with an asymmetrical distribution.

570

1982 02 22 06 Z (M10240, T [K])



571

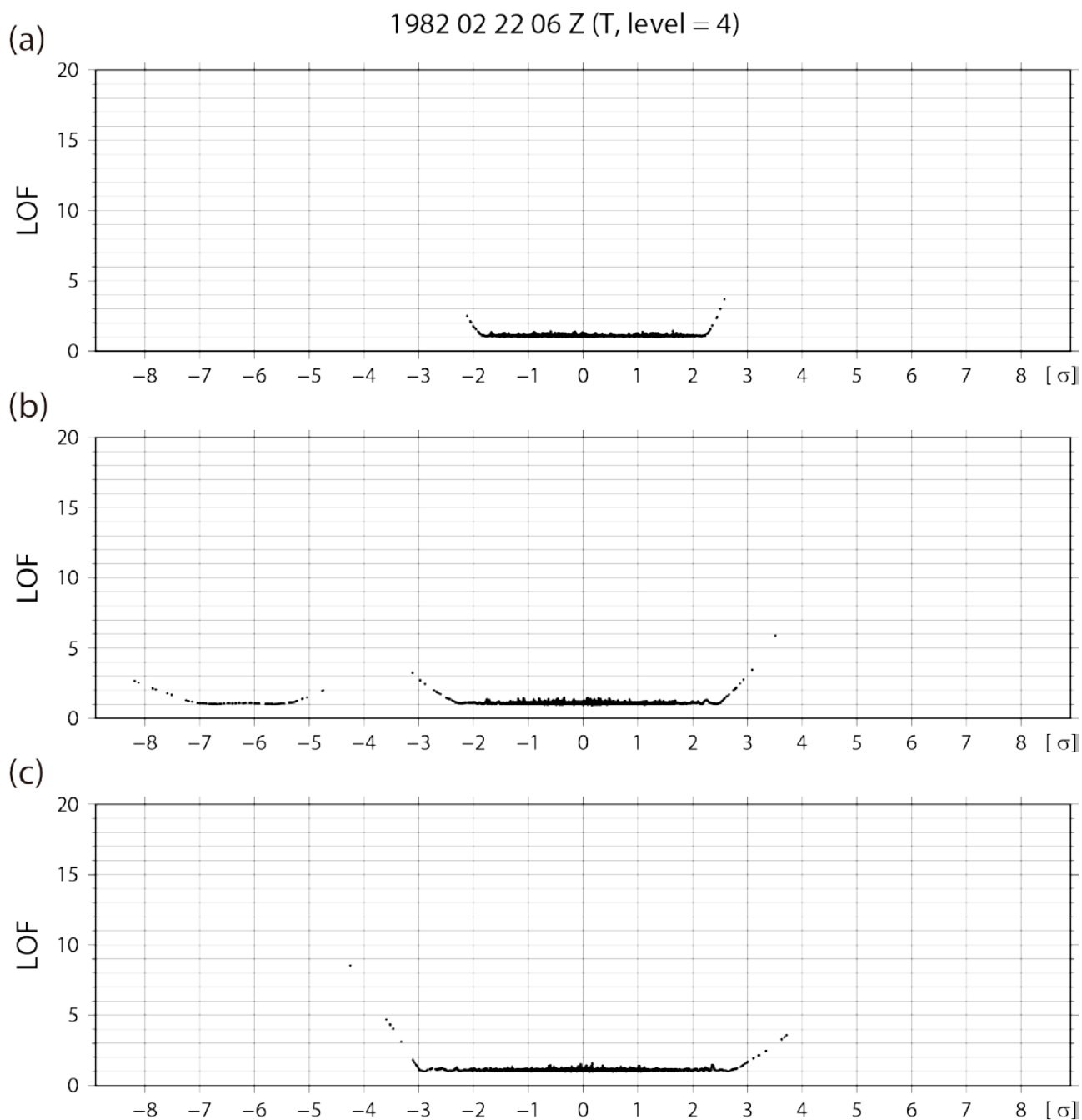
572

573

574

575

Figure 4: Spatial distributions of (a) analysis absolute error, (b) analysis ensemble spread, (c) background skewness, (d) background kurtosis, and (e) background KL divergence for temperature at the fourth model level (~500 hPa) at 0600 UTC 22 February. Contours indicate geopotential height of the ensemble mean at the 500 hPa level.



576

577 Figure 5: Scatter diagrams of the local outlier factor method (*LOF*) versus distance from the

578 ensemble mean for all ensemble members for background temperature at the fourth model level

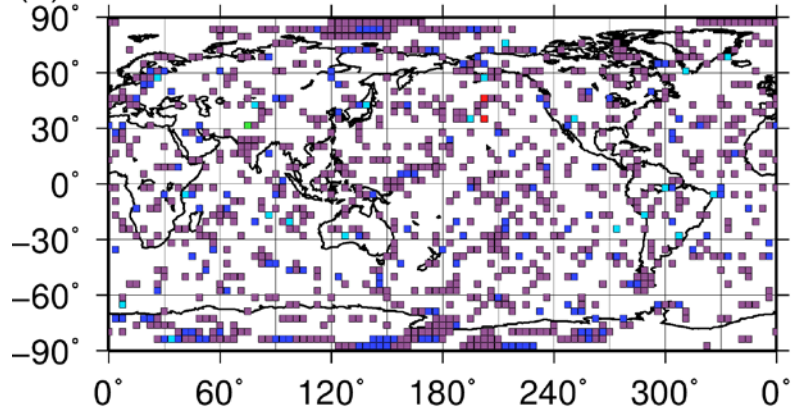
579 (~500 hPa) at (a) grid point A (16.7°S, 90.0°E), (b) grid point B (35.3°N, 146.3°E), and (c) grid

580 point C (35.3°N, 112.5°W).

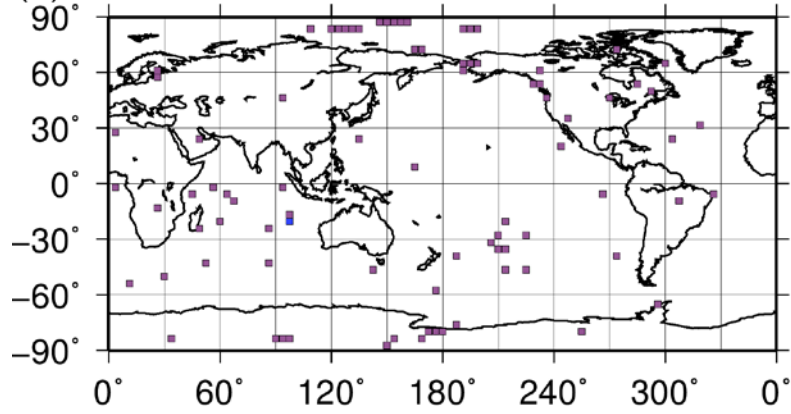
581

Number of Outliers (T, Level = 4)

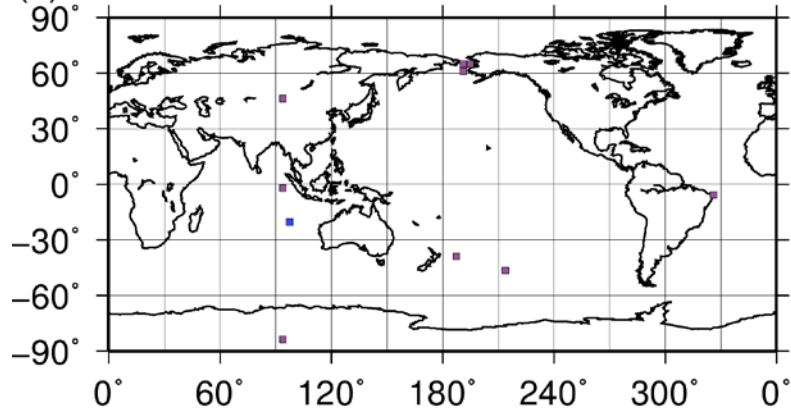
(a) LOF value > 5.0



(b) LOF value > 8.0



(c) LOF value > 11.0

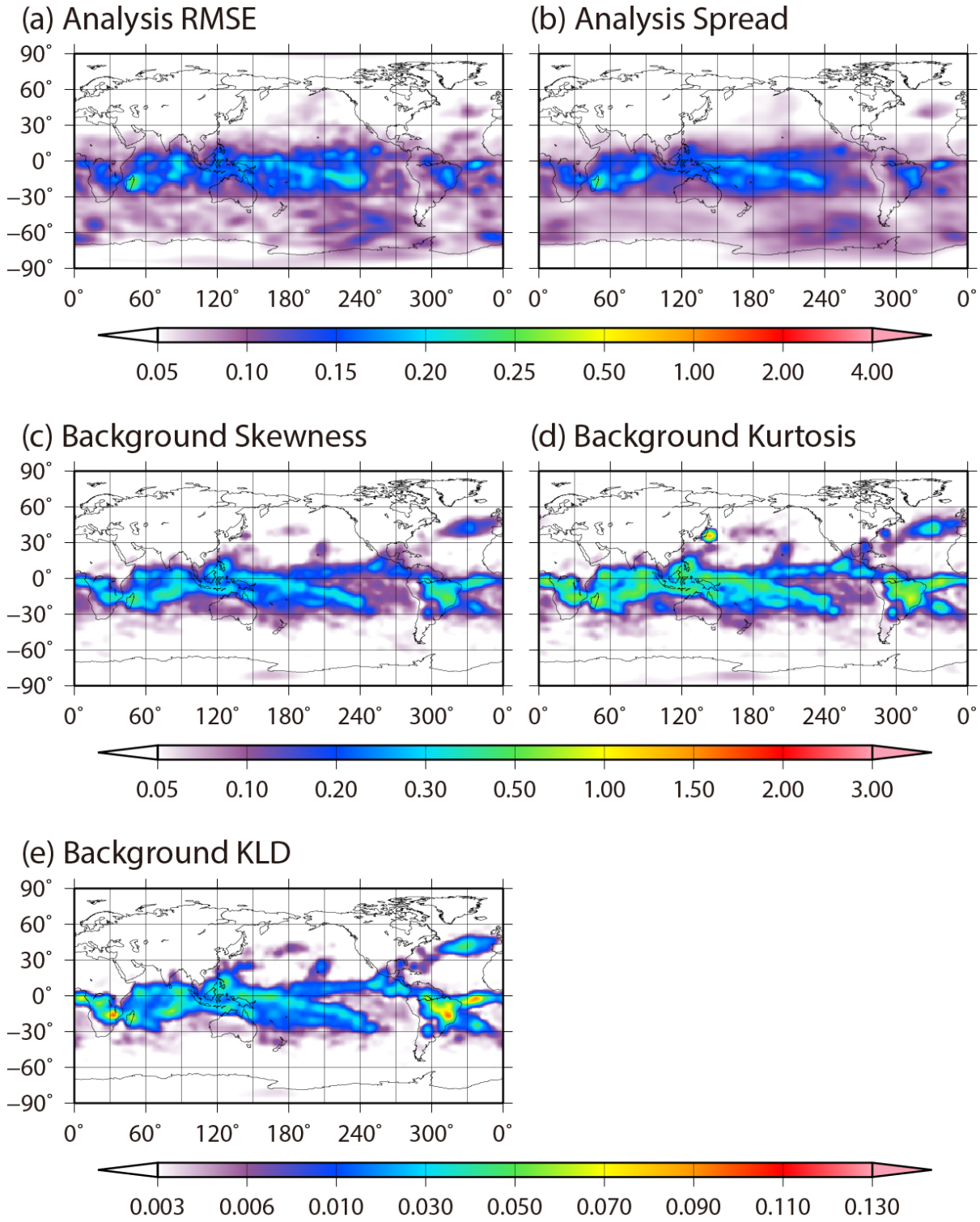


582

583 Figure 6: Spatial distributions of the number of outliers for background temperature at the fourth

584 model level (~500 hPa) at 0600 UTC 22 February for *LOF* thresholds of (a) 5.0, (b) 8.0, and (c)

585 11.0.



586

587

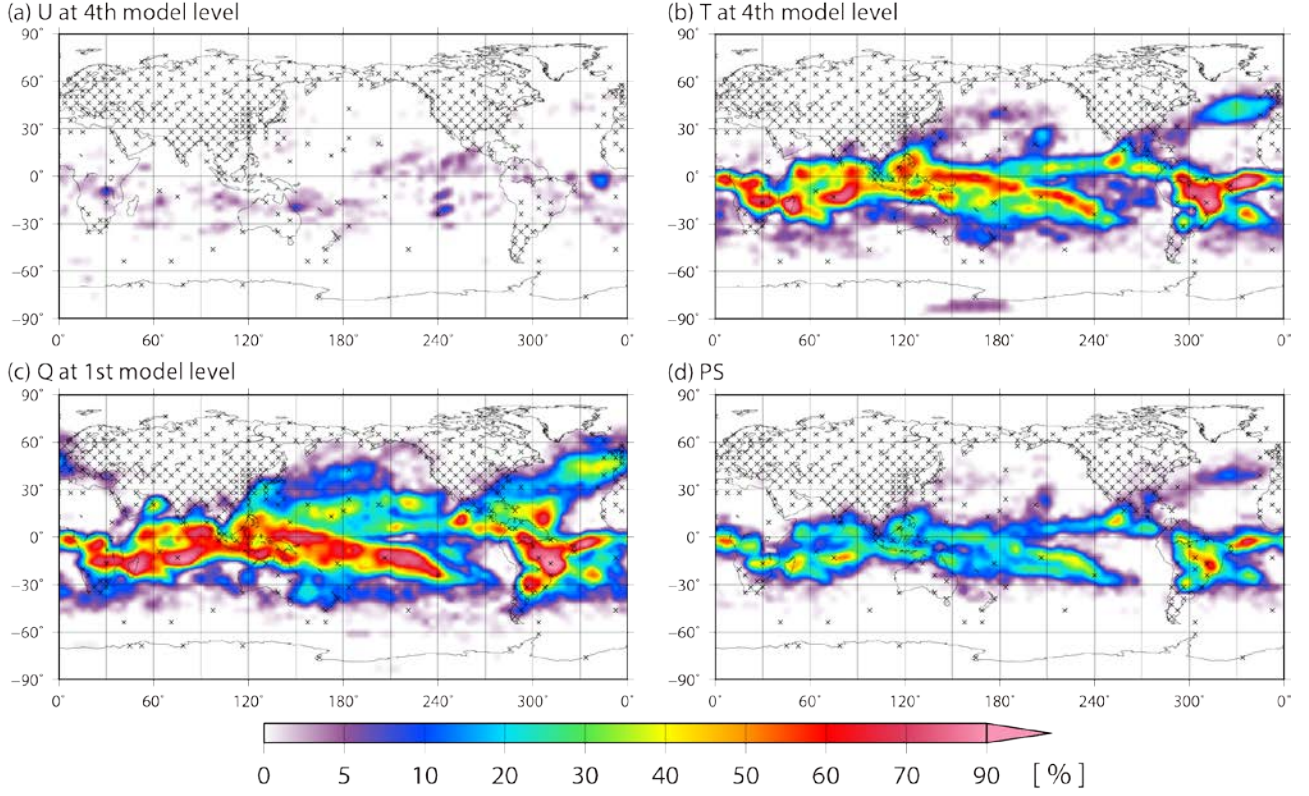
588

589

590

Figure 7: Spatial distributions of the time-mean (a) analysis RMSE, (b) analysis ensemble spread, (c) background absolute skewness, (d) background absolute kurtosis, and (e) background KL divergence for temperature at the fourth model level (~500 hPa) from 0000 UTC 25 January to 1800 UTC 1 March.

Frequency of Non-Gaussianity



591

592

593

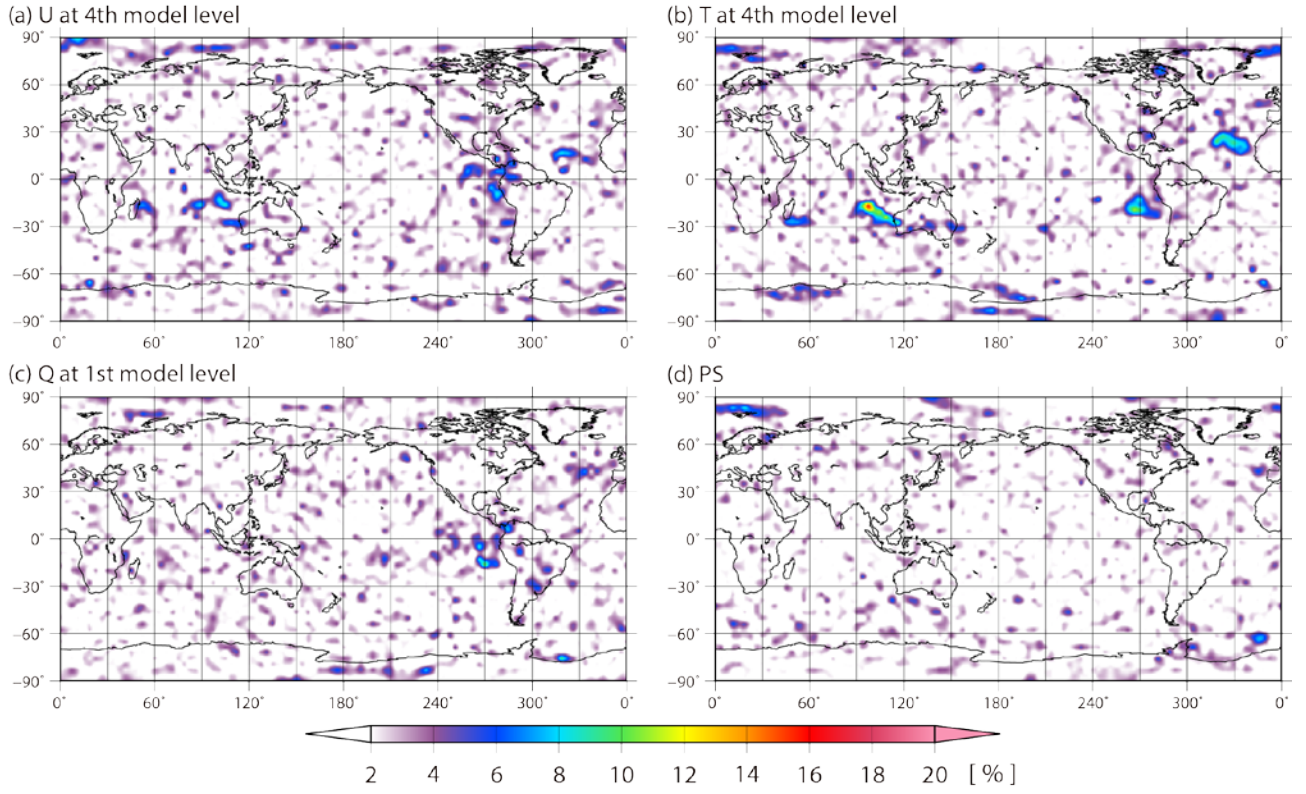
594

595

596

597

Frequency of Outlier

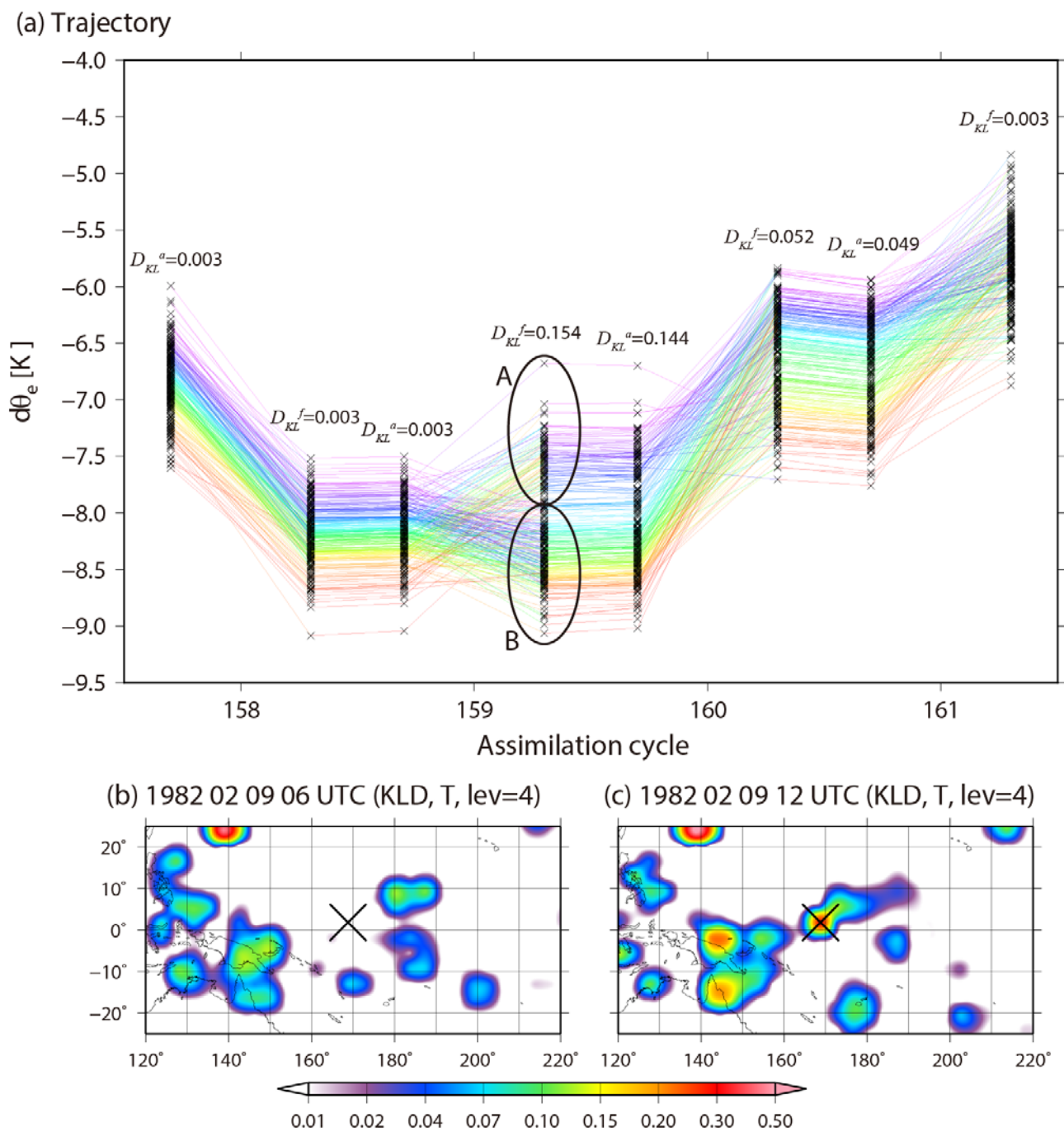


598

599 Figure 9: Similar to Fig. 8, but showing the frequency of identifying at least one outlier with high

600 $LOF > 8.0$ on a 10240-member ensemble.

601



602

603 Figure 10: Lifecycle of non-Gaussianity at 1.9°N, 168.7°E. (a) Trajectories of 256 randomly chosen

604 members from 10240 members for $d\theta_e$ (see text for definition) from analysis at the 157th analysis

605 cycle (0000 UTC 9 February) to forecast the 161st analysis cycle (0000 UTC 10 February). The

606 colors show the order of $d\theta_e$ for every analysis. D_{KL} shows KL divergence for $d\theta_e$, and the

607 superscripts a and f indicate analysis and forecast, respectively. (b, c) Spatial distributions of KL

608 divergence for background temperature at the fourth model level (~500 hPa) at the 158th analysis
609 cycle (0600 UTC 9 February) and the 159th analysis cycle (1200 UTC 9 February), respectively.
610 The cross shows the location of the point considered in panel a.

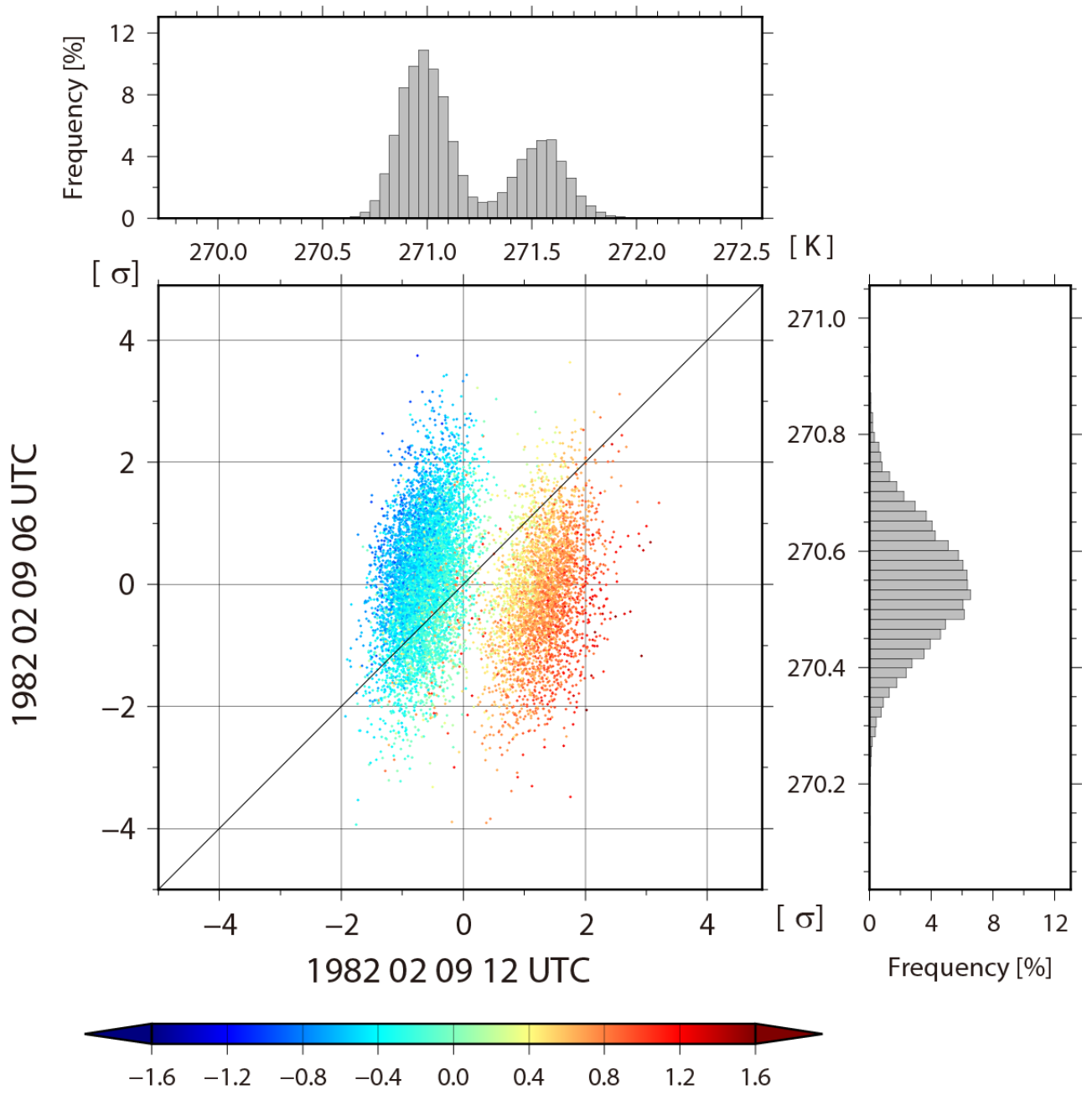
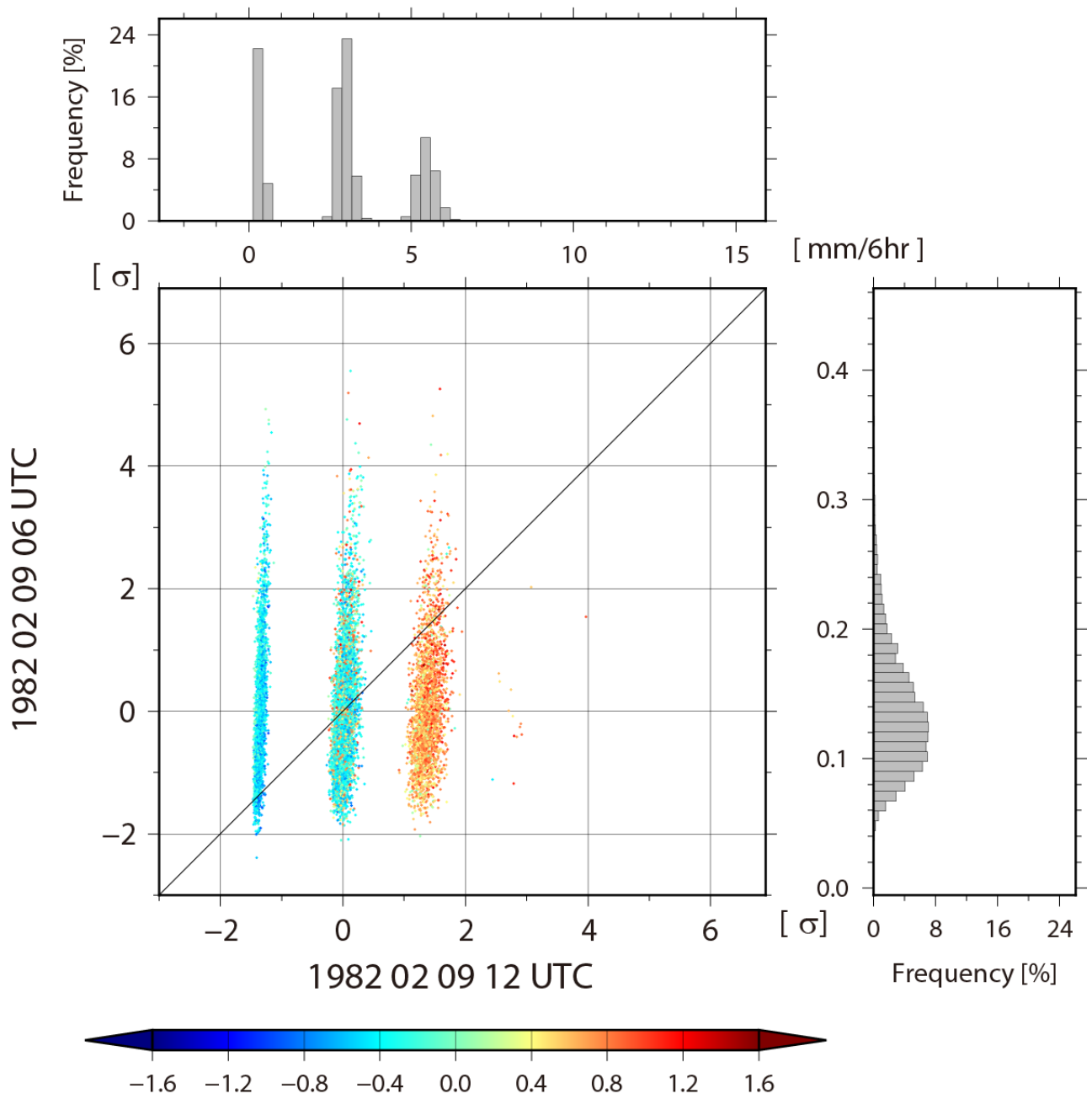


Figure 11: Scatter diagram of 0600 UTC versus 1200 UTC 9 February for the background temperature at the fourth model level (~ 500 hPa) at 1.9°N , 168.7°E . The colors show $d\theta'_e = (d\theta_{e\ 1200\ \text{UTC}} - d\theta_{e\ 0600\ \text{UTC}}) - (d\bar{\theta}_{e\ 1200\ \text{UTC}} - d\bar{\theta}_{e\ 0600\ \text{UTC}})$. The histograms on the right side and upper side show the background temperature at the same grid point.

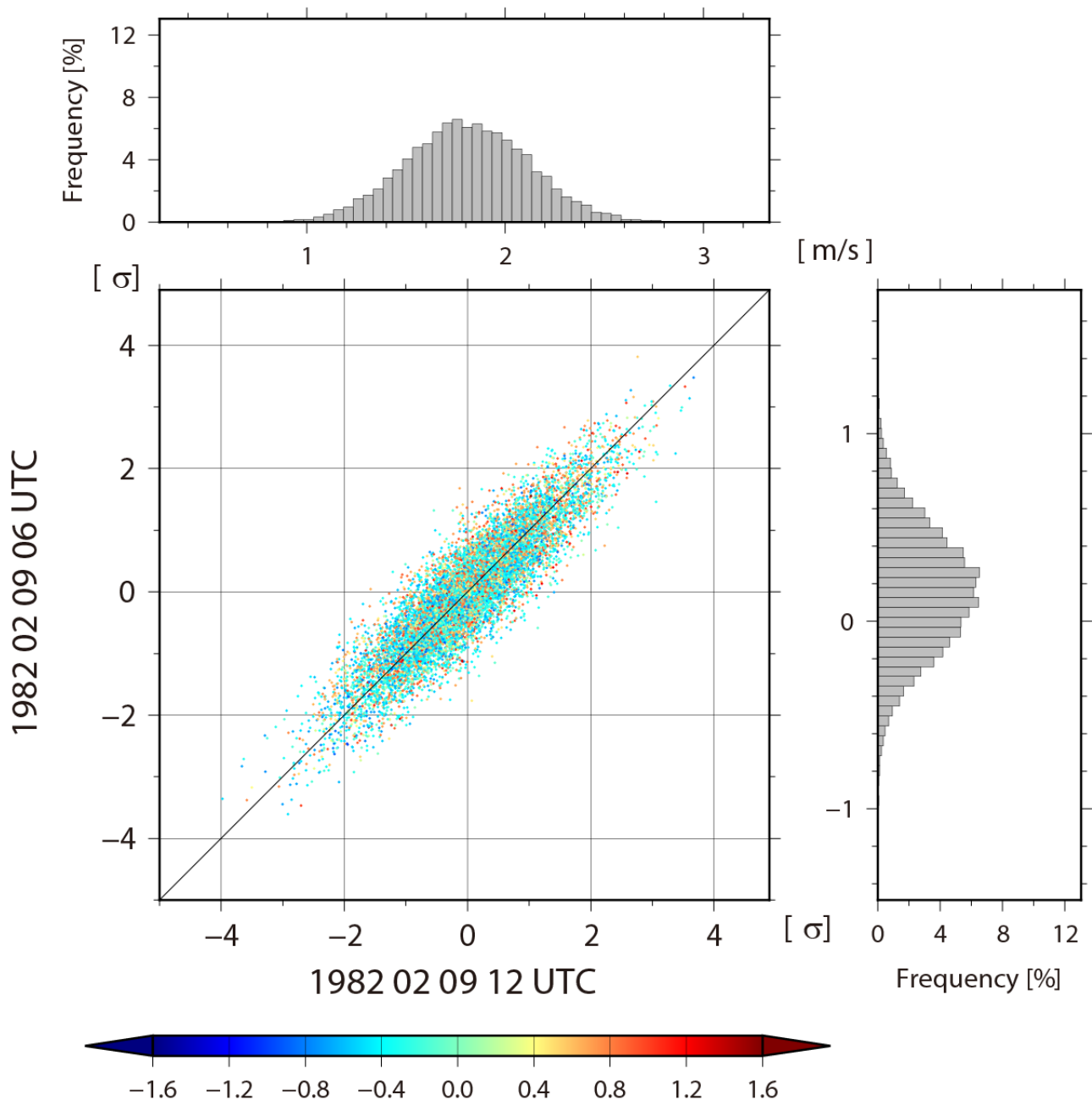


617

618 Figure 12: Similar to Fig. 11, but for 0600 UTC versus 1200 UTC 9 February for background

619 precipitation.

620



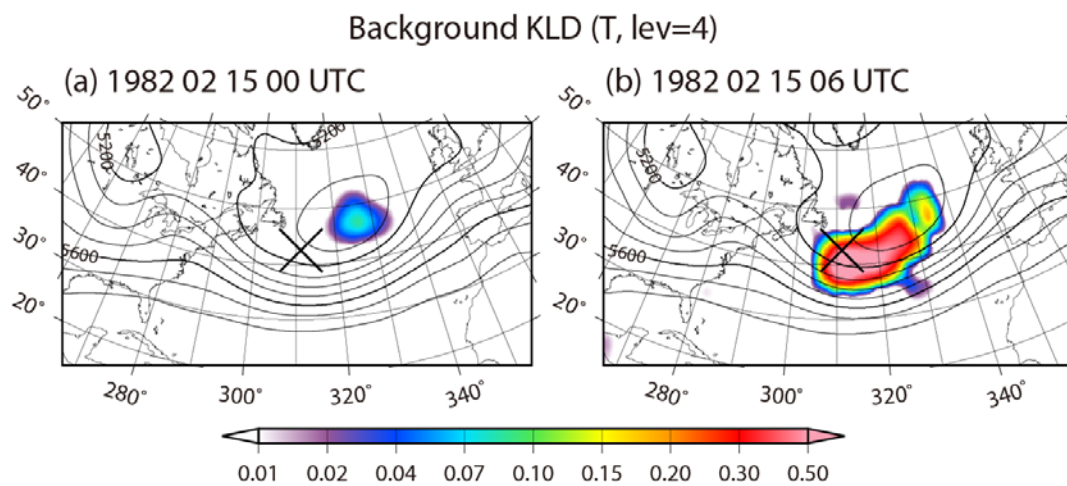
621

622 Figure 13: Similar to Fig. 11, but for 0600 UTC versus 1200 UTC 9 February for background zonal

623

wind at the fourth model level (~500 hPa).

624



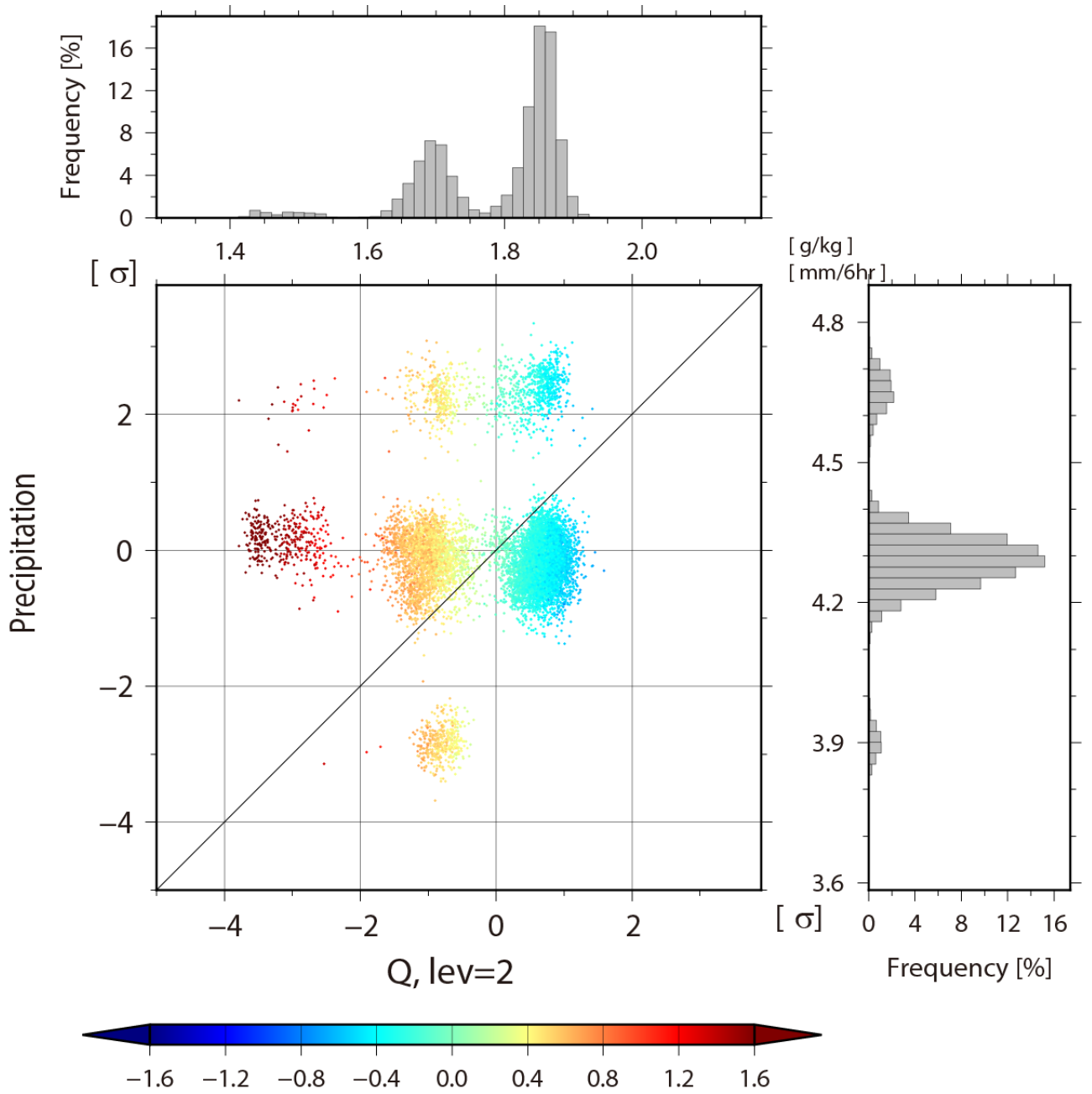
625

626 Figure 14: Spatial distributions of the KL divergence for background temperature at the fourth

627 model level (~500 hPa) (a) at 0000 UTC 15 February and (b) at 0600 UTC 15 February. Contours

628 show geopotential height of the ensemble mean at the 500 hPa level.

629



630

631 Figure 15: Scatter diagram of background specific humidity at the second model level (~850 hPa)

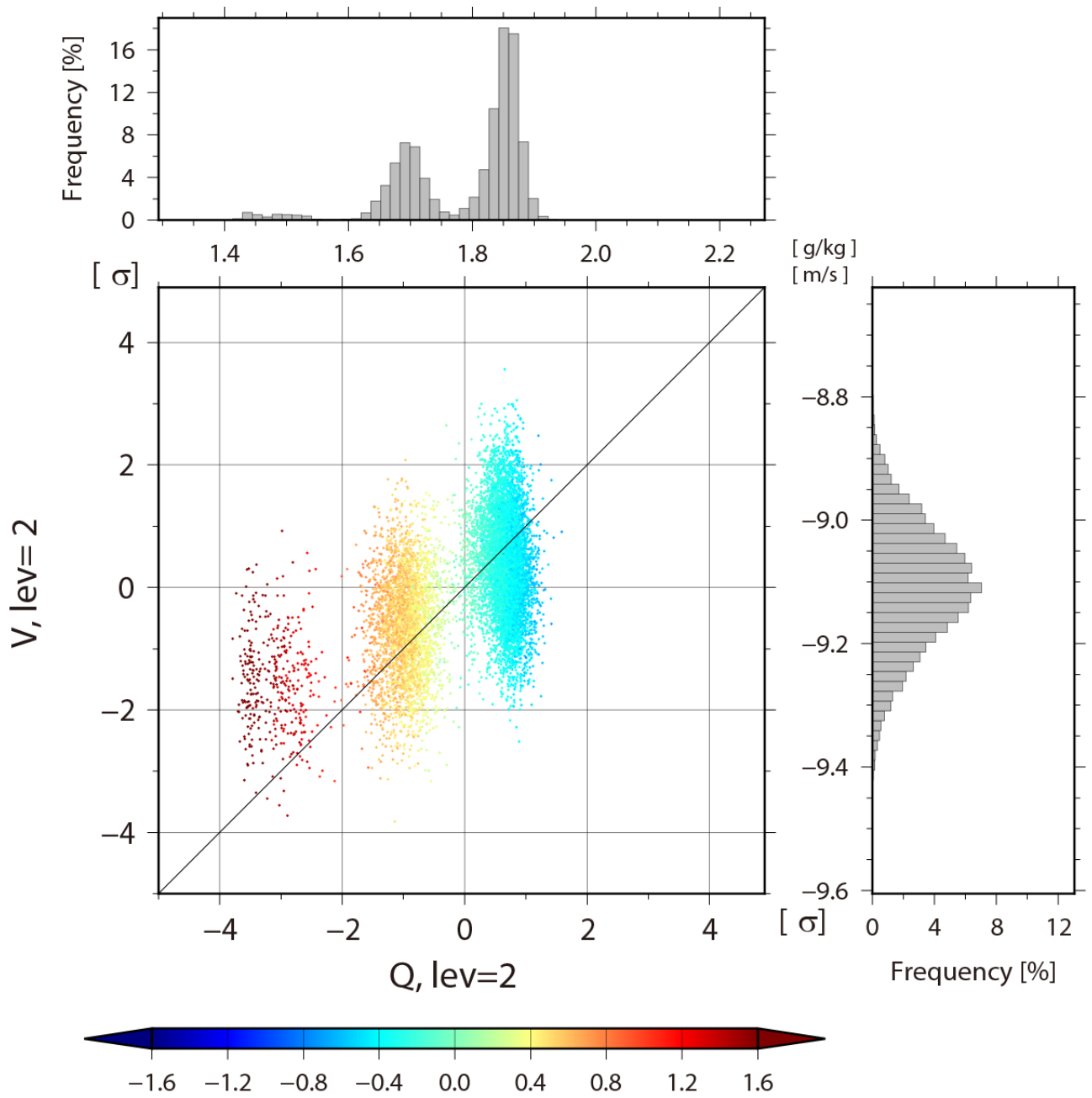
632 versus background precipitation at 42.7°N, 48.8°W (311.3°E) at 0600 UTC 15 February. The colors

633 show $d\theta'_e = (d\theta_{e\ 0600\ UTC} - d\theta_{e\ 0000\ UTC}) - (d\bar{\theta}_{e\ 0600\ UTC} - d\bar{\theta}_{e\ 0000\ UTC})$. The histograms on the

634 right side and on top show background precipitation and temperature at the same grid point,

635 respectively.

636

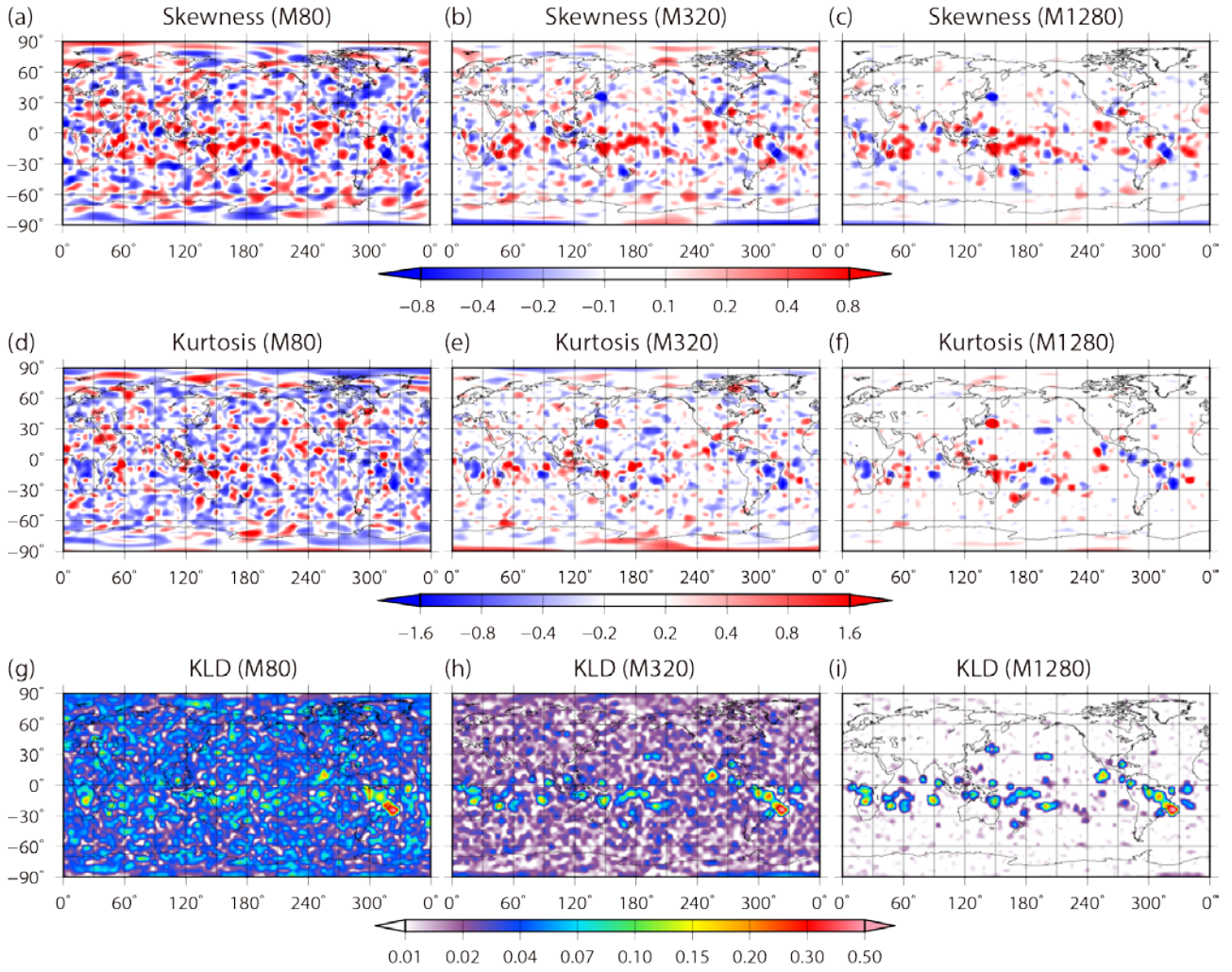


637

638 Figure 16: Similar to Fig. 14, but for background specific humidity versus meridional wind

639 background at the second level (~850 hPa).

640



641

642

643

644

645

Figure 17: Spatial distributions of (a-c) skewness, (d-f) kurtosis, and (g-i) KL divergence for temperature at the fourth model level (~ 500 hPa) at 0600 UTC 22 February. The left, center, and right columns show 80, 320, and 1280 subsamples from 10240 members, respectively.

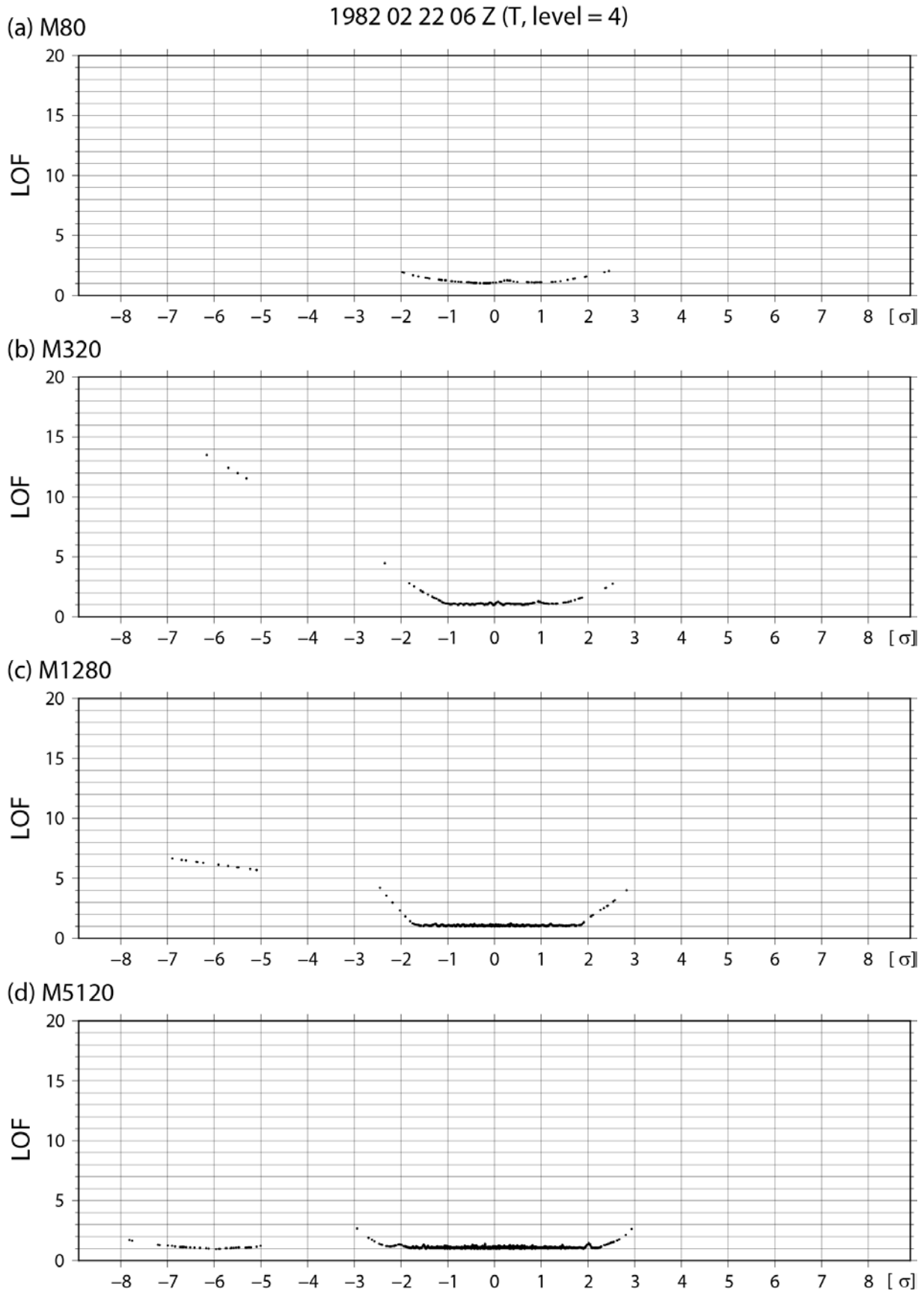
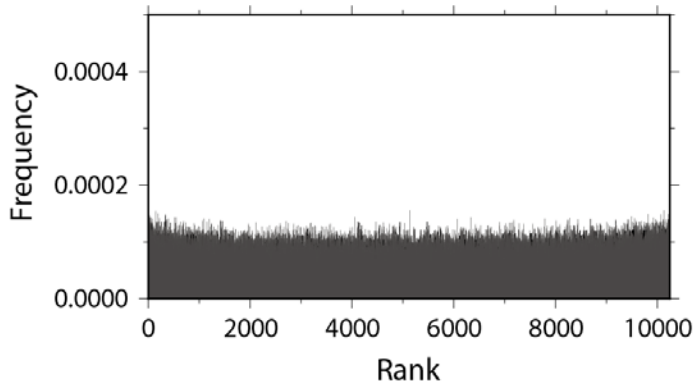


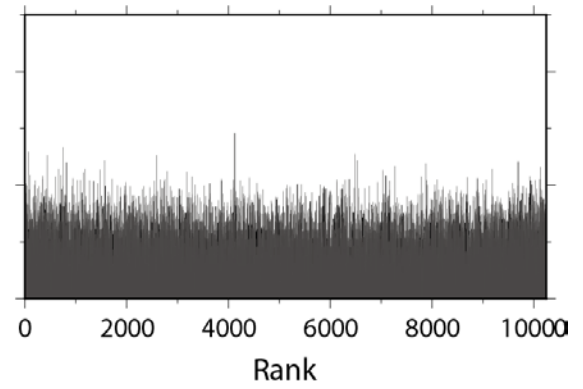
Figure 18: Similar to Fig. 5b, but for the ensemble sizes (a) 80, (b) 320, (c) 1280, and (d) 5120.

Rank Histogram (Q, Level = 1)

(a) All grid points



(b) Grid points with non-Gaussian PDF



649

650 Figure 19: Rank histograms verified against truth for background specific humidity at the lowest

651 model level (~925 hPa) at (a) all grid points and (b) the grid points with non-Gaussian PDF from

652 0000 UTC 25 January to 1800 UTC 1 March.

653

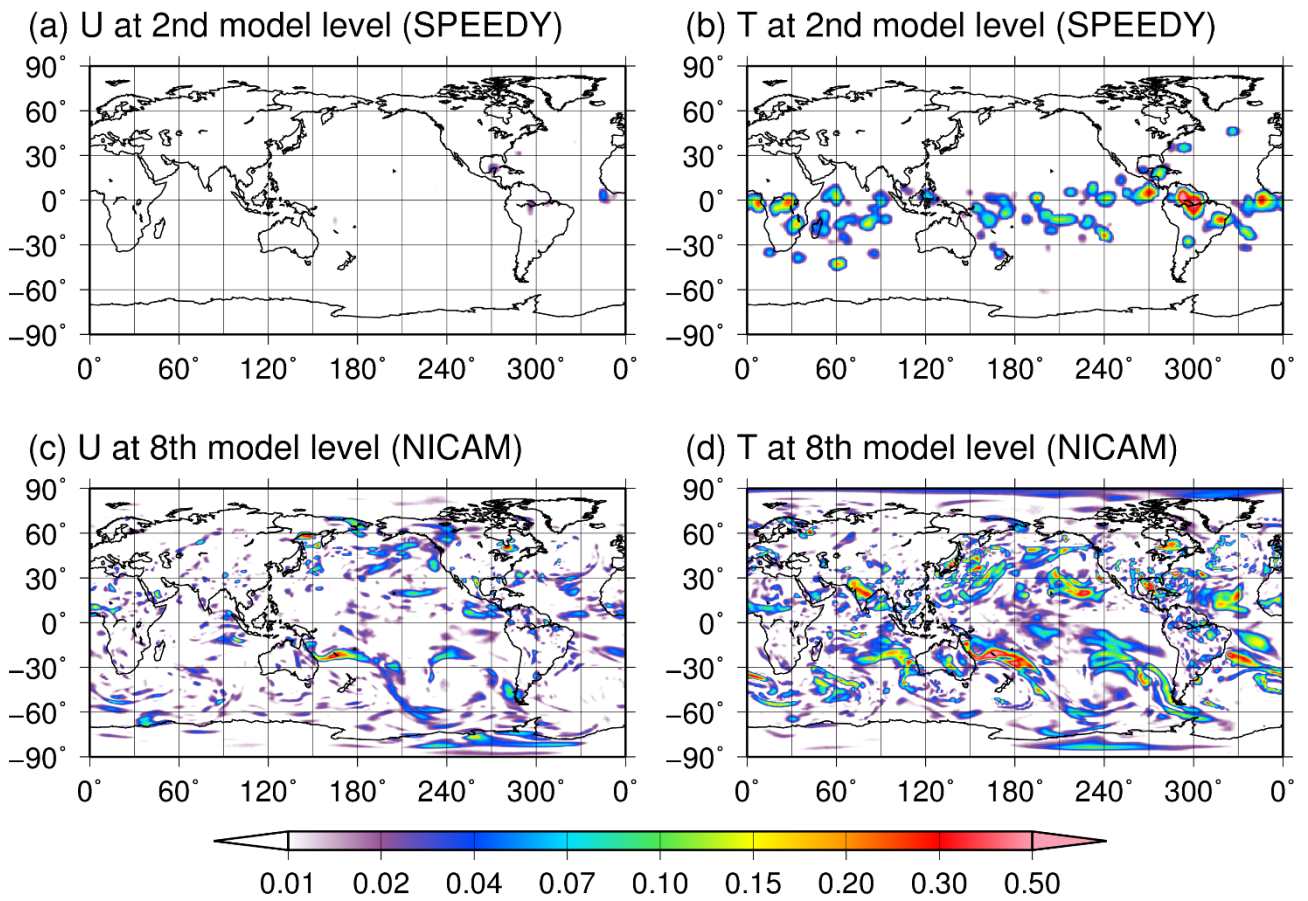


Figure 20: Spatial distributions of background KL divergence for SPEEDY model and NICAM.

Upper panels show (a) zonal wind and (b) temperature at the second model level (~ 850 hPa) for the SPEEDY model at 0000 UTC 1 March. Bottom panels show (c) zonal wind and (d) temperature at the eighth model level (~ 850 hPa) for NICAM at 0000 UTC 8 November 2011.

660 Table. 1: CRPS and its three components (reliability, resolution and uncertainty) for background
661 specific humidity at the lowest model level (~925 hPa) from 0000 UTC 25 January to 1800 UTC 1
662 March.

	CRPS [g kg ⁻¹]	Reli [g kg ⁻¹]	Resol [g kg ⁻¹]	<i>U</i> [g kg ⁻¹]
All grid points	0.0214	0.0000101	0.525	0.547
Grid points with non-Gaussian PDF	0.0475	0.0000244	0.030	0.077

663